Focused Ion Beam Induced Deposition of Copper

by

Anthony D. Della Ratta

B.S., Materials Science and Engineering,
Cornell University (1991)

Submitted to the Department of Materials Science and Engineering in partial fulfillment of the requirements for the degree of

Master of Science
in Materials Science and Engineering

at the

MASSACHUSETTS INSTITUTE OF TECHNOLOGY

June, 1993

ARCHIVES
MASSACHUSETTS INSTITUTE
OF TECHNOLOGY
JUL 30 1993
LIBRARIES

© Massachusetts Institute of Technology 1993. All rights reserved.

Author ....
Department of Materials Science and Engineering
May 7, 1993

Certified by ....
John Melngailis
Principal Research Scientist
Thesis Supervisor

Certified by ....
Carl V. Thompson
Professor of Electronic Materials
Thesis Supervisor

Accepted by ....
Linn W. Hobbs
Chair, Departmental Committee on Graduate Students
John F. Elliott Professor of Materials

Focused Ion Beam Induced Deposition of Copper

by

Anthony D. Della Ratta

Submitted to the Department of Materials Science and Engineering
on May 7, 1993, in partial fulfillment of the
requirements for the degree of
Master of Science
in Materials Science and Engineering

Abstract

As the dimensions of integrated circuits decrease into the submicron range, the problems of circuit delay and interconnect reliability become more urgent. Due to its low resistivity (1.67 $\mu\Omega$-cm) and high electromigration resistance, copper has received attention as a candidate metal for the integrated circuits of the future. In addition, the focused ion beam, with its capability for milling and deposition at linewidths of 0.1 μm or below, has proved useful as a tool for integrated circuit "microsurgery". Focused ion beam induced deposition of copper from a novel organometallic precursor compound, Cu(hfac) TMVS, has been achieved using 25 to 35 keV Ga^+ ions from a liquid metal ion source. Submicron copper lines deposited at room temperature from this precursor exhibit resistivities as low as 50 $\mu\Omega$-cm; a sharp drop in these values is noted for deposition at 70°C, and deposition on a substrate heated above about 100°C yields resistivities near those of pure bulk copper. Composition analysis by Auger Electron Spectroscopy shows the high temperature deposition to be nearly pure copper. Deposition yields of 28 atoms per incident Ga^+ ion have been obtained on both silicon and silicon dioxide substrates, with growth rates of up to 2.2 nm per second at an average ion current density of 200 $\mu A/cm^2$. The quality and microstructure of the deposited film seems to be inextricably tied to the ability of the carbon-containing byproduct molecules to desorb from the growing film. Low impurity concentrations and low resistivities are found at low ion current densities or high temperatures, conditions which allow greater byproduct desorption. Under the proper conditions, this particular precursor compound shows great promise for use in the focused ion beam induced deposition of low resistivity, submicron interconnects on integrated circuits for repair processes.

Thesis Supervisor: John Melngailis
Title: Principal Research Scientist

Thesis Supervisor: Carl V. Thompson
Title: Professor of Electronic Materials

Acknowledgments

I would like to take this opportunity to thank those who have given me the support to carry out this research. I am particularly indebted to my advisors Dr. John Melngailis and Professor Carl V. Thompson for their guidance. Their helpful advice and encouragement made this thesis work possible. Professor Klavs Jensen of the Department of Chemical Engineering at MIT is responsible for suggesting this particular copper precursor to our research group, and Dr. John A.T. Norman of Schumacher Company in Carlsbad, Calif. is to be thanked for providing us with the compound. We are grateful to FEI Company of Beaverton, Ore. for loaning us a focused ion beam milling system, and for the guidance of Rufus Knapp at FEI in installing and operating it. The U.S. Army Research Office supplied the funding for this project under contract DAAL 93-90-G-0223. I learned much from Dr. Xu Xin, who was very helpful in acquainting me with the focused ion beam machinery and general laboratory procedures, and with whom I had many enlightening discussions. I would also like to thank Dr. Carey Pico, who was patient enough to impart to me his knowledge of TEM sample preparation, and Christian Musil, who provided me with a copy of the TRIM ion implantation simulation program. Thanks also go to Elizabeth Shaw of the Surface Analysis Facility at the Center for Materials Science and Engineering for Auger Electron Spectroscopy compositional analysis and to Mike Frongillo for training in transmission electron microscopy. I am also grateful to Young-Chang Joo, Lisa Su, Heather Inglefield, Brett Knowlton, Roland Carel, Robert Lescanec, Christian Honeker, and Tony Chiang for their technical assistance and companionship. Last, but not least, I would also like to acknowledge the love and support of my parents and sister. Without their patience and kind words, this thesis would have been more difficult to complete.

Contents

1 Introduction **13**

1.1 Photolithography 13

1.2 Submicron Ion Beam Patterning 16

1.2.1 Overview of Focused Ion Beam Technology 16

1.2.2 Focused Ion Beam Lithography 24

1.2.3 Focused Ion Beam Induced Deposition 25

1.3 Objectives 33

1.4 Summary 34

2 Equipment and Materials **35**

2.1 Focused Ion Beam 35

2.2 Copper Precursor 39

2.3 Auger Electron Spectroscopy (AES) 41

2.4 Resistivity Measurements 44

2.5 Profilometry 45

2.6 Scanning Electron Microscopy 45

2.7 Transmission Electron Microscopy 46

2.8 Summary 48

3 Experimental Procedures **50**

3.1 Yield Experiments 50

3.1.1 General Deposition Procedure 50

3.1.2 Current Density Dependence 51

3.1.3 Gas Pressure Dependence 52
3.1.4 Dwell Time Dependence 52
3.1.5 Measurement and Calculation 53
3.2 Resistivity 53
3.2.1 Temperature Dependence 53
3.2.2 Current Density Dependence 54
3.2.3 Dwell Time Dependence 55
3.3 Gas Pressure at the Sample 55
3.4 TEM Sample Preparation 57
3.5 Auger Electron Spectroscopy 58
3.6 Summary 58

4 Results and Discussion **60**

4.1 Local Gas Pressure 60
4.2 Yield and Growth Rate 62
4.2.1 Average Current Density Dependence 62
4.2.2 Temperature Dependence 65
4.2.3 Dwell Time Dependence 66
4.2.4 Pressure Dependence 68
4.3 Resistivity 69
4.3.1 Average Current Density Dependence 69
4.3.2 Temperature Dependence 72
4.3.3 Dwell Time Dependence 74
4.4 Composition 75
4.4.1 Temperature Dependence 75
4.4.2 Average Current Density Dependence 76
4.5 Microstructure 77
4.5.1 High Aspect Ratio Lines 77
4.5.2 Temperature Dependence 78
4.5.3 Average Current Density Dependence 81

4.5.4 Dwell Time Dependence 85
4.5.5 Precursor Pressure Dependence 85
4.5.6 Sidewall Deposition 88
4.6 Summary 89

5 Conclusions and Future Work **90**
5.1 Summary and Conclusions of this Work 90
5.2 Future Work 92

Bibliography **94**

List of Figures

1-1 Subtractive etching using positive and negative resists. (ref. 1) . . . 14

1-2 Schematic diagram of a typical focused ion beam system (ref. 17) . . 17

1-3 Plot of beam current versus distance from beam axis (ref. 12) 20

1-4 Opaque and clear defects in lithographic masks (ref. 16) 22

1-5 FIB differential channelling contrast image of grains in an aluminum thin film. (FEI Company) 23

1-6 Focused ion beam induced deposition, illustrating the adsorption of gas molecules on the surface and their dissociation either by excited surface atoms or by a thermal spike. 26

1-7 Plan view of gold films deposited from DMG(hfac) using 40 kV Ga+ FIB (ref. 28) 29

1-8 (a) Ion flux, (b) gas adsorbate density, and (c) deposition and sputtering as a function of time (ref. 29) 30

1-9 Results of a yield vs. dwell time experiment using 30 kV Ga^+ ions at a current density of 8.6 A/cm^2 to dissociate $W(CO)_6$ gas molecules. (ref. 29) 31

2-1 The IBT Dubilier Focused Ion Beam system, with custom made work chamber. (ref. 27) 36

2-2 The FEI FIB 500D Focused Ion Beam Milling System (FEI Company) 37

2-3 Gas manifold for introduction of Cu(hfac)TMVS precursor into the work chamber. 39

2-4 (a) Copper(+1) hexafluoroacetylacetonate trimethylvinylsilane, a.k.a. Cu(hfac)TMVS, and (b) vapor pressure characteristics (ref. 30,31) . . 40
2-5 Types of transitions occurring in electron shells when struck by an energetic electron. (ref. 32) 42
2-6 Auger Electron Spectroscopic data displayed in derivative form. (ref. 32) 43
2-7 Four point probe measurement for resistivity determination. (ref. 34) 44
2-8 Block diagram of the lens and detector system in a scanning electron microscope. (ref. 35) 46
2-9 Diagram of a typical transmission electron microscope (TEM) and optical analogue. (ref. 35) 47

3-1 Finger pattern used for four point probe resistivity measurements. . . 54
3-2 Schematic arrangement for stagnation tube experiment to measure local precursor gas pressure. To measure the pressure, valves 1,2, and 4 are left open and valves 3 and 5 are closed. 56
3-3 Preparation of silicon nitride membranes for TEM. 57

4-1 Graph of Cu(hfac)TMVS precursor pressure measured as a function of distance from the mouth of the capillary tube via a stagnation tube and capacitance manometer. 61
4-2 Yield data in atoms per incident gallium ion, assuming the film has the density of pure bulk copper, on silicon and silicon dioxide substrates, as a function of average current density of deposition. The films were deposited using 35 keV Ga^+ at room temperature, at an estimated copper precursor pressure of approximately 1.5 mtorr. 62
4-3 Growth rate in angstroms per second plotted as a function of the average ion current density. The depositions were made using 35 keV Ga^+ at room temperature at a gas precursor pressure of 1.5 mtorr at the point of ion incidence. 64

4-4 Deposition yield as a function of deposition temperature. The gas precursor pressure was about 1.5 mtorr and the average ion current density was 20 μA/cm^2, using 35 keV Ga$^+$. 65

4-5 Dependence of the deposition yield on the ion beam dwell time. The depositions were all carried out using 35 keV Ga$^+$ at room temperature at a local precursor pressure of 1.5 mtorr. The average ion current density was varied as indicated in the graph. 67

4-6 The deposition yield as a function of the local precursor gas pressure at the point of ion incidence, as measured via the stagnation tube experiment for two different experimental runs. The current density was 40 μA/cm^2 and the films were deposited using 35 keV Ga$^+$ at room temperature. 68

4-7 Resistivity of copper lines deposited on tungsten finger patterns (described in Chapter 3) versus average ion current density during deposition. The precursor pressure was approximately 1.5 mtorr at the sample surface and the lines were deposited at room temperature with 35 keV Ga$^+$. The resistivity of pure bulk copper is 1.67 $\mu\Omega$-cm. . . . 69

4-8 Resistivity plotted versus growth rate, illustrating the the decreasing conductivity trend. The local gas pressure was 1.5 mtorr and the lines were deposited at room temperature with 35 keV Ga$^+$. 70

4-9 Effect of increasing deposition temperature on the film resistivity. The resistivity at the highest temperature is approximately 2 $\mu\Omega$-cm, close to the value for pure copper (1.7 $\mu\Omega$-cm). The films were deposited at a local precursor pressure of about 1.5 mtorr at an average ion current density of 20 μA/cm^2 using 35 keV Ga$^+$. 73

4-10 Effect of varying dwell time on resistivity of copper depositions using 35 keV Ga$^+$. The local gas pressure was approximately 1.5 mtorr, at an ion current density of 40 μA/cm^2. The two curves show the results of two experimental runs. 74

4-11 Composition of copper films deposited using 35 keV Ga^+ at various sample temperatures. The gas pressure was 1.5 mtorr during deposition, and the ion current density was 20 $\mu A/cm^2$. 75

4-12 Composition of copper films deposited at various average ion current densities, as determined using Auger Electron Spectroscopy. The local precursor pressure was approximately 1.5 mtorr, and the films were deposited at room temperature with 35 keV Ga^+. 76

4-13 SEM micrographs of copper lines deposited at an ion current density of (a) 110 $\mu A/cm^2$ and (b) 128 $\mu A/cm^2$ using 25 keV Ga^+. 77

4-14 Electron diffraction pattern from a film deposited with 25 keV Ga^+ at 80°C, at a precursor pressure of 1.5 mtorr and an ion current density of 20 $\mu A/cm^2$. 78

4-15 TEM micrographs of approximately 50 nm thick FIBID copper films deposited using 25 keV Ga^+ at (a) room temperature, (b) 40°C, (c) 67°C, (d) $80°C$, and (e) 100°C. The average current density during deposition was 20 $\mu A/cm^2$ of 25 keV Ga^+ at a local precursor pressure of about 1.5 mtorr. 79

4-16 SEM micrographs of FIBID copper films illustrating the roughening of the surface at higher deposition temperatures using 35 keV Ga^+. (a) room temperature, (b) 66°C (c) 78°C (d) 100°C. The films were deposited at an ion current density of 20 $\mu A/cm^2$ at a precursor pressure of 1.5 mtorr. 82

4-17 TEM micrographs of approximately 50 nm thick FIBID copper films deposited with 25 keV Ga^+ at average ion current densities of (a) 10 $\mu A/cm^2$, (b) 50 $\mu A/cm^2$, and (c) 200 $\mu A/cm^2$. The films were deposited at room temperature at a local precursor pressure of 1.5 mtorr. 83

4-18 SEM micrographs of FIBID copper films deposited with 35 keV Ga^+ at different average ion current densities, illustrating the surface morphology. (a) 20 $\mu A/cm^2$, (b) 50 $\mu A/cm^2$, and (c) 200 $\mu A/cm^2$. The films were deposited at room temperature at a local precursor pressure of 1.5 mtorr. 84

4-19 TEM micrographs of approximately 50 nm thick FIBID copper films deposited at ion beam dwell times of (a) 100 ns and (b) 2.2 μs The films were deposited at room temperature at a current density of 20 $\mu A/cm^2$, at a local precursor pressure of 1.5 mtorr 86

4-20 TEM micrographs of approximately 50 nm thick FIBID copper films deposited at local Cu(hfac)TMVS pressures of (a) 2.6 mtorr (b) 1.5 mtorr and (c) 0.25 mtorr. The films were deposited at room temperature at a current density of 20 $\mu A/cm^2$. 87

4-21 Example of periodic comb-like structure as the ion beam deposits on a nearly vertical sidewall. The line was deposited at room temperature at an ion current density of 250 $\mu A/cm^2$. 88

List of Tables

4.1 Schematic representation of regions of high and low resistivity as a function of current density $< J >$ and substrate temperature T. The circles represent low resistivity (20 $\mu\Omega$-cm and below), the x's represent high resistivity (150 $\mu\Omega$-cm and above), and the circled x's represent resistivities between these two values. 71

4.2 Comparative Deposition Characteristics at an Average Ion Current Density of 250 $\mu A/cm^2$. 72

Chapter 1

Introduction

In recent years, focused ion beams (FIB) have proved useful in a wide variety of different applications related to fabrication, modification, and analysis of materials on the submicron scale. More specifically, this technique has found widespread use in microelectronic circuit repair, in which thin films of conductors and insulators less than half a micron in width may be cut and deposited to exacting tolerances. The FIB provides a means to insert jumpers or create open circuits at strategic points on an integrated circuit; in this way a chip which is initially faulty due to missing interconnects or shorts may be repaired and thus salvaged. This thesis focuses on one aspect of this "microsurgery," the production of connectors or jumpers by the deposition of a conducting material, in this particular case, copper. This introductory chapter provides an overview of conventional submicron patterning techniques and the uses of the FIB in deposition and milling in microelectronics, and finally highlights the major objectives of this thesis research.

1.1 Photolithography

The traditional means of patterning the thin films of conductors and insulators necessary for integrated circuit fabrication is through the process of photolithography.[1, 2, 3] In a typical subtractive photolithographic process, a thin film of polymer or other patternable material called photoresist is coated or spun on the surface of the

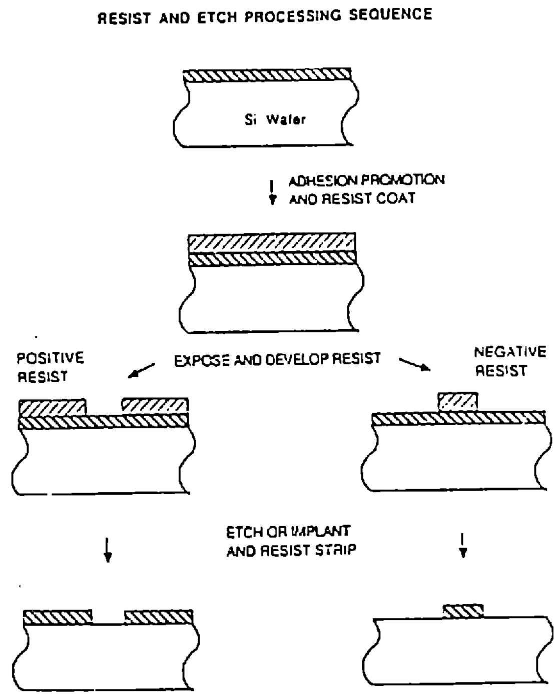

Figure 1-1: Subtractive etching using positive and negative resists. (ref. 1)

film to be patterned. A mask is interposed between a source of typically short wavelength electromagnetic radiation and the resist-coated film. The mask contains the pattern information to be eventually transferred to the film by the radiation via the resist layer in a manner which depends on the type of resist used. In a positive resist, the areas of the resist exposed to incident radiation will be dissolved away in the subsequent development and dissolution stage and uncover the underlying film in the exposed areas. In a negative resist, those areas of the resist unexposed to the radiation will not be dissolved away in this stage and the underlying film will remain covered in the exposed areas. Following the development and dissolution of the resist is the etch step, in which removal of the underlying film only occurs on those areas uncovered by resist. After this step, the resist layer has outlived its usefulness and is stripped. The patterning of thin films by the subtractive etch process, which is most prevalent in integrated circuit manufacture, is illustrated in figure 1-1.

An example of an additive photolithographic process would be the fabrication of X-ray masks using gold absorbing material. The photoresist layer is spun on top of a

very thin layer of the metal, called a plating base, and patterned such that the base is exposed in selected areas. Then gold electroplating is performed, with the result that the metal will only grow where the base is exposed to the plating solution. The resist is then stripped once the desired pattern of metal has been formed.

The ultimate resolution of photolithographic processes can be described using the Raleigh criterion for resolution, expressed in the following form:

$$d = k\frac{\lambda}{NA} \tag{1.1}$$

where d is the smallest resolvable feature, k is a constant, λ is the wavelength of the radiation, and NA is the numerical aperture, defined as the sine of one half of the acceptance angle of the lens. The constant k depends on the type of photoresist used and also on the method of exposure. The lowest and hence best k's (as low as 0.5) could be obtained using a positive photoresist and contact printing, in which the photomask used to define patterns of light and dark on the resist is placed in intimate contact with the resist-coated wafer. Somewhat higher k's are obtained from negative resist formulations and the use of proximity printing, in which the photomask is held close to but not in contact with the wafer. It is predicted that perhaps the use of deep UV excimer lasers ($\lambda = 193$ nm) will permit the imaging of sub-quarter micron features, but this seems to be the lower limit on feature size for photolithography. The Raleigh criterion may also be expressed alternatively as

$$DOF = k'\frac{\lambda}{NA^2} \tag{1.2}$$

In this form, DOF represents the depth of focus, or that distance over which the gap between mask and wafer may be varied while maintaining image focus on the wafer. The symbol k' is another constant. It is easily seen that as the wavelength is reduced or the numerical aperture is increased to produce smaller features, it becomes more difficult to maintain focus on a wafer with relatively severe topography. It is more desirable to decrease the wavelength to attain the small image size than to increase NA due to the strong dependence of the depth of focus on the latter, and this has

stimulated interest in deep UV and X-ray lithography. [1, 4]

Various issues come into play concerning the photoresist formulation. Positive resists usually consist of a polymer and photoactive compound, or PAC, in a resin, typically novolac based. This resin tends to absorb short λ radiation and presents a problem in the deep UV regime. The PAC acts as a dissolution inhibitor and is sensitive to the imaging radiation. Upon exposure, the PAC actually becomes a dissolution enhancer, and the resist is removed in the exposed areas upon development. For a negative photoresist, the exposure causes crosslinking of individual polymer chains, thus drastically increasing the molecular weight of the polymer and preventing dissolution of the exposed areas. As mentioned previously, positive photoresists like PMMA (an electron and ion beam resist) tend to have greater resolving power than certain negative resists, since the latter polymers tend to swell in the developing solution.[1, 4]

1.2 Submicron Ion Beam Patterning

The use of ion beams for patterning features on microelectronic circuitry received increasing attention once it became possible to reduce or focus the diameter of the beam impinging on the target to the order of microns and below.[5, 6, 7, 8, 9] Initial attempts used electrostatic lenses to focus the beam, but the first real breakthrough came with the invention of the field ionization source. With the emergence of the relatively stable and long-life liquid metal ion source (LMIS), focused ion beam technology became a viable tool for patterning and modification at the submicron scale. The following sections detail some general considerations in the use of focused ion beam (FIB) technology, and the application of FIB to lithography and the deposition and removal of conducting materials.

1.2.1 Overview of Focused Ion Beam Technology

The major parts of a typical FIB system are diagrammed schematically in figure 1-2. The LMIS provides the ions used in the apparatus and also to a large degree deter-

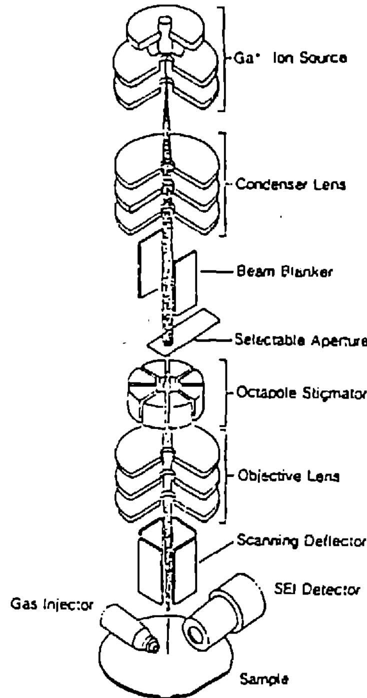

Figure 1-2: Schematic diagram of a typical focused ion beam system (ref. 17)

mines the final beam diameter. An extraction electrode in proximity to the source provides the electrostatic field necessary to ionize the metal atoms and draw them from the the LMIS. Electrostatic lenses are used, with a movable aperture to regulate the beam current to the sample. An ion pump or equivalent is used to maintain the column pressure below 10^{-7} torr to minimize contamination of the source. Typically, the ion column just described is separated from the main work chamber by a differential pumping aperture; in this way the source life can be maximized by maintaining a low pressure in the column as gases are introduced into the work chamber, which is typically the case when ion beam induced deposition or etching is carried out, as will be explained later.

As hinted at above, perhaps the most critical component of an FIB system is the source of ions. The focused spot sizes which can be produced from the field ionization sources and liquid metal ion sources (LMIS) are far smaller (on the order of tens to hundreds of angstroms) than a focused broad beam of ions from a conventional ion implanter source, which can achieve dimensions of a few microns at best. The two

main types of sources will be described below.

The field ionization source[7, 8] consists of a fine tungsten needle held at cryogenic temperatures. Placed in an atmosphere of hydrogen or helium, it can develop very high electric fields at its tip and serves as a very bright source of these light ions. The LMIS[5, 6] is similarly also a fine tungsten needle, but wet with some pure metal or metal alloy. If the metal is not liquid at room temperature, the source is usually heated during operation to melt the source material and wet the needle. Perhaps the brightest and most stable LMIS is the pure gallium source, which is widely used in commercial FIB milling systems employed in microelectronics failure analysis labs. The operation of the LMIS source is rather complex and depends on a balance of electrostatic forces, which extract the Ga^+ ions, and hydrostatic forces, which limit the flow of liquid metal. At the very tip, a so-called Taylor cone of metal, of a radius near 10 nm, is formed; the optimum cone angle for ion emission is near 50 degrees. Although the cone tip is rather small, in actuality the virtual source is rather larger, perhaps ten times so, mostly due to space charge repulsion of the ions. This effect is typically greater for more massive ions, and it also gives rise to the so-called chromatic aberration by introducing a spread in energies, ΔE, about the nominal energy for the ions.

The actual beam size obtained in the FIB as the ions strike the sample is typically from 0.05 μm to 0.2 μm. This is largely due to the effect of aberration in the column and the space charge effect mentioned earlier. The chief aberration in the ion beam column is chromatic, in which ions of different energies are focused at different points on the ion optical axis. It follows that heavier ions would be subject to a stronger chromatic aberration than lighter ions due to their greater ΔE. The actual expression for the increase in beam spot size d_c due to this aberration in the ion column is

$$d_c = C_c \alpha \frac{\Delta E}{E} \tag{1.3}$$

where α is half the angle of the beam, and C_c is the chromatic aberration coefficient. It is apparent that increasing the beam voltage leads to a decrease in beam size.

Another beam-broadening effect is the spherical aberration, which is typically much less severe than the previous effect. Here, the ions passing through a lens further from the axis are focused more strongly than those passing through closer to the axis. The resultant beam broadening d_s is given by

$$d_s = \frac{C_s \alpha^3}{2} \tag{1.4}$$

where C_s is the spherical aberration coefficient. The space charge effect gives rise to a further broadening d_o, so that the total beam size d can be expressed as

$$d = \sqrt{d_o^2 M^2 + d_c^2 + d_s^2} \tag{1.5}$$

where M is the magnification. Typically the beam size in FIB is limited by chromatic aberration.[9, 10]

An important aspect of the focused ion beam which must be considered in cutting, deposition, or implantation operations is the presence of beam skirts. As seen in figure 1-3, a small yet significant current extends some distance from the primary, high current portion of the beam.[11] If the aim is to implant only a relatively narrow strip, the presence of a current 100 times less than the main current and which may extend for up to 3 μm radially from the center of the beam may need to be taken into consideration. The effect is thought to arise from the source itself, and it is possible that some combination of lens configuration and apertures may help reduce its importance.

The interaction of ion beams with the target atoms warrants discussion. As the ion travels through the material it loses energy in collisions both with electrons and atomic nuclei. In colliding with nuclei of mass M_2, the ratio K of the energy E of the reflected ion of mass M_1 to the incident ion energy E_o is given by

$$K = \frac{E}{E_o} = \left(\frac{(M_2^2 - M_1^2 \sin^2\theta)^{1/2} + M_1 \cos\theta}{(M_1 + M_2)}\right)^2 \tag{1.6}$$

where θ is the angle between the incident and reflected ion paths. The result of

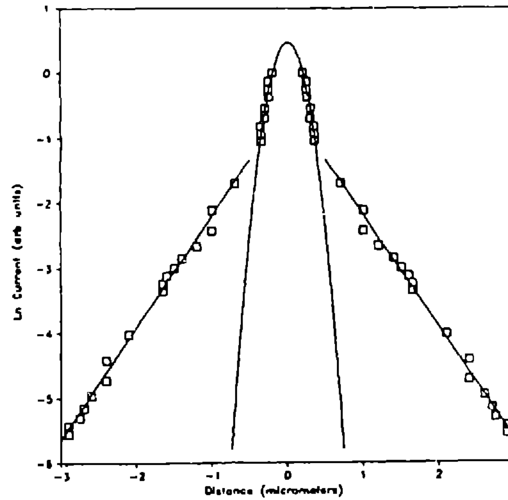

Figure 1-3: Plot of beam current versus distance from beam axis (ref. 12)

bombardment of a substrate material with ions of sufficiently high energy (above about 100 keV) is significant implantation of the ions in an approximately Gaussian distribution of concentration with depth; a more realistic fit is given by a so-called Pearson IV distribution, containing asymmetry (skewness) and flatness (kurtosis) parameters. The depth of implant, or range, is controlled by the acceleration potential and by the nuclear and electronic stopping power of the material. The total dose, or number of ions implanted per unit area, is given by integrating the current over time, and dividing by the ion charge and the area rastered. The width of the implant both in the directions parallel and perpendicular to the incident ion path is described by a longitudinal and lateral straggle, respectively. It must be noted that the actual penetration depth is a function of the crystalline orientation of the substrate, with certain directions (e.g. $< 110 >$ in silicon) providing "tunnels" for the ions to traverse much deeper into the sample than for a randomly aligned target with no paths for preferential ion transport. The result is a long "tail" on the distribution of the implant which can cause an implanted junction to occur more deeply than originally intended.

The implant can cause a high degree of damage consisting of point defects distributed spatially in the same way as the implanted ions, and results in amorphization at high doses. This damage is typically readily annealed out, leaving a doped, crystalline layer when the appropriate ion species are implanted. Typically, a rapid thermal anneal is used, in which the sample is briefly heated at a high temperature for a period long enough for lattice repair to occur but short enough to prevent significant dopant diffusion. It is possible to carry out longer heating excursions if one takes into account the overall broadening in the nearly-Gaussian implant profile; by calculating this change one can fabricate p-n junctions at a controlled depth into a semiconductor wafer, for instance. Less energetic ions typically induce mostly sputtering or ion milling, which is the removal of surface atoms due to the ion collision. Typically the sputtered atoms have energies from 50 eV to 1 keV, and are removed at a rate, or sputtering yield, of 1-10 atoms per incident ion. In addition, very low energy secondary electrons are emitted from the surface at about the same yield as the sputtered atoms; these are detectable in the focused ion beam machinery by such instruments as channel electron multipliers (CEMs), and provide a means of viewing the sample during ion bombardment. [9]

The use of the focused ion beam to effect highly localized ion sputtering or milling is another useful feature of the technique. Unlike ion milling using a broad beam extending almost several square millimeters or so over the sample, effects such as redeposition of sputtered material and self-focusing must be considered in FIB milling, where the beam diameter in this case is only 0.2 μm or less. Redeposition occurs when material removed by the ion beam from the point of ion incidence is ejected normally from the milled surface to deposit on other surfaces. This often necessitates repeated scans of an area to remove the redeposited material. This effect, however, may be exploited if it is desired to bridge two closely neighboring conductors with redeposited metal, as has been demonstrated.[13] The self-focusing effect tends to lead to narrow cuts that taper with depth in the substrate at high ion doses, probably due to the enhanced sputter yield at the more glancing angles of the trench near the bottom.[14] Perhaps this effect could also be utilized to produce extremely narrow cuts which

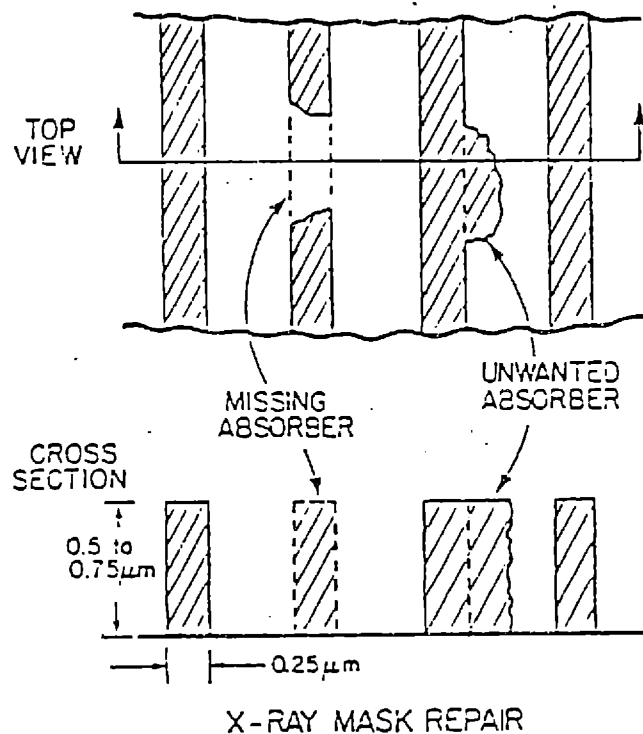

Figure 1-4: Opaque and clear defects in lithographic masks (ref. 16)

cannot be obtained at the surface using conventional milling techniques.[15]

Some examples of the use of milling and cutting by the focused ion beam in practical situations occur in mask repair and integrated circuit microsurgery. The FIB is typically quite useful for the repair of defects in X-ray masks, for example. These types of masks are analogous to the chrome-on-glass photomasks described above in the section on photolithography, except that they usually consist of patterns delineated in some high atomic number, X-ray absorbing material deposited on a thin silicon or silicon nitride membrane. Typically, the X-ray absorbing material is a metal like gold or tungsten which must be made both narrow enough to attain a small feature size, and yet also thick enough to block the X-rays. It is difficult to fabricate such high aspect ratio features reliably, and these types of masks often have clear and opaque defects (figure 1-4). The opaque defects can be milled away, obviating repetition of the complete mask fabrication procedure. Clear defects can be repaired via focused ion beam induced deposition, in which the ion beam is used to dissociate adsorbed gas molecules containing the metal to be deposited, allowing the user to

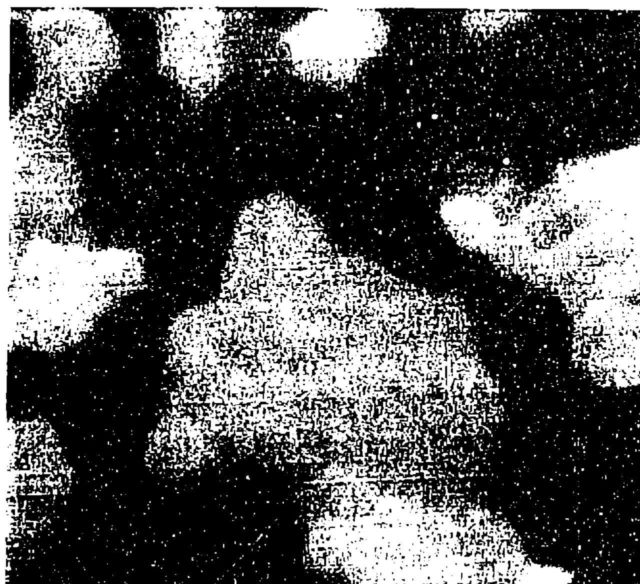

Figure 1-5: FIB differential channelling contrast image of grains in an aluminum thin film. (FEI Company)

simply "write in" an absorbing, high aspect ratio structure at the submicron scale. The theory of the process of focused ion beam induced deposition, with which this thesis deals, is discussed in more detail in a later section.

Another useful feature of the focused ion beam is its ability to reveal the grain structure of polycrystalline films. Grains in the film appear as a mosaic of light and dark patches due to differential channelling contrast in a video representation of the secondary electron yield (figure 1-5). As discussed previously, certain crystalline orientations allow energetic ions to travel much further into the sample than if the sample were amorphous or aligned in some random orientation with respect to the incident ion beam. If the ions are channelled, fewer secondary electrons are liberated by the ion in its passage, since it is interacting with fewer atoms in the target material. As a result, those grains which are aligned in low index directions (such as $< 111 >$ or $< 110 >$) tend to channel the incoming ions more than other more random orientations, and hence appear dark when the secondary electron signal is collected

and transformed into an image. Studies have been made of the relative secondary electron yields from different grain orientations in several basic crystal structures, providing a means for quantitatively differentiating between grain types. This may be useful in monitoring the growth of certain orientation grains in thin films, as in preferential secondary grain growth. This type of crystallographic information is not obtainable in a conventional scanning electron microscope, since the incoming electron beam in this case only yields topographical data, which can be quite misleading in attempts to determine the true grain structure of a film. Typically the sample should be viewed at several angles around normal incidence to ensure that multiple grains are differentiated and that two or more grains are not interpreted as a single grain on the video image. Although the resolution of the FIB is significantly poorer than that of the SEM, the crystallographic contrast this instrument reveals makes the FIB an ideal tool for examining the grain structure in submicron metal interconnects for integrated circuits which may be likely to pose reliability problems, as in the highly microstructure-dependent failure phenomenon of electromigration.[17]

1.2.2 Focused Ion Beam Lithography

One of the major uses of the focused ion beam is for lithographic patterning. While in photolithography, radiation is used to expose the photoresist in selected areas, in FIB lithography the ions are used to chemically alter the resist in specific patterns. The photolithographic process is a rapid, parallel process in which many interconnect patterns can be exposed at once, while the analogous ion beam process is a much slower, serial process. However, the small diameter of the beam allows a rather smaller linewidth to be patterned than that possible using light or deep ultraviolet radiation, and FIB lithography has received attention as means for producing the sub-quarter micron feature sizes of the future. [18, 19] In addition, the ion beam process is maskless, which reduces the cost and complexity of the lithographic process.

A typical resist used for FIB lithography is the positive resist PMMA (polymethylmethacrylate), used also in electron beam lithography. Upon exposure with electrons or ions, the solubility of the exposed resist is enhanced. Typically, the total ion charge

or dose required to achieve a certain exposure level is significantly less than the total electron charge needed. In addition, light ions, such as helium or hydrogen from a field ionization source, tend to traverse into the resist with a minimum of scattering normal to the incident path, whereas electrons scatter much more, leading to a pattern dependent exposure known as the proximity effect. One disadvantage of FIB lithography is that typically the electrons travel much further into the resist, whereas the more massive ions do not penetrate as far. Consequently, resist thicknesses in ion lithography are restricted to less than a micron.

Inorganic resists have also been investigated. Films of materials like chromium, aluminum, or cermets are deposited and exposed using the ion beam. A plasma or wet etch then follows, either etching the implanted or unimplanted regions of the resist, depending on the material used. For instance, the chromium is implanted with antimony and then etched in a CCl_4 plasma, and the aluminum is implanted with arsenic or antimony, and then etched using H_3PO_4.[20, 21] It is also possible to use this method to pattern these types of conductors directly from a blanket film of metal.

1.2.3 Focused Ion Beam Induced Deposition

As mentioned in the discussion of X-ray mask repair, the FIB is a useful tool to carry out deposition of conductors at the small scales required on these types of masks and also on integrated circuits. The concept of focused ion beam induced deposition of a material is illustrated in figure 1-6. Gas molecules containing atoms of the material to be deposited are introduced to the point of ion incidence, usually by means of either a capillary tube or by placing the sample in a small enclosure within the main work chamber such that the ion beam can still strike the sample; a gaseous ambient in the millitorr pressure range is maintained in the box while preserving a relatively low vacuum in the work chamber.

Considerable effort has been expended in isolating the mechanism for the ion induced deposition. Two distinctly different models have been considered [22, 23] for the focused ion beam induced deposition of gold from the compound DMG(hfac). Both models have been compared with experimental results. In both cases, the gaseous

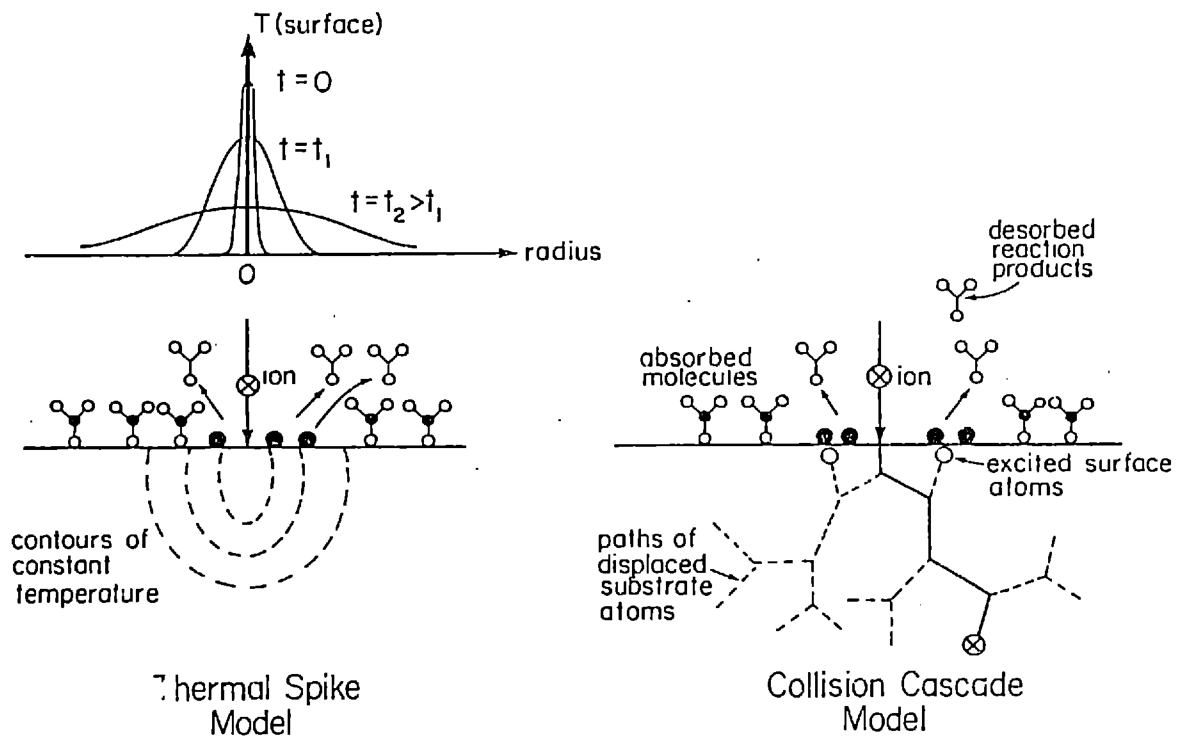

Figure 1-6: Focused ion beam induced deposition, illustrating the adsorption of gas molecules on the surface and their dissociation either by excited surface atoms or by a thermal spike.

precursor is assumed to adsorb on the surface in a monolayer. In addition, no further adsorption is presumed to occur during the ion/target interaction, which seems reasonable considering typical gas flow rates and ion fluxes. The film on which deposition is considered to occur is that of the deposited metal, in this case gold; once the first few tens of nanometers are deposited, the growth is essentially occurring on the metal.

The first theory involves the thermal spike created by the ion in the target material; this model employs a delta function rise in temperature at the time of ion impact, and the spatially expanding temperature distribution is followed as a function of time. It assumes that the small volume of material surrounding the point of ion impact is a continuum through which heat flows, when in actuality it is composed of discrete atomic particles. The thermal distribution was modelled as a hemispherical flow of heat from the initial instantaneous deposition of energy in a point at the surface at time $t = 0$, and also as an axially symmetric cylindrical flow of heat from an instantaneous line source. The spike temperature is tracked starting at t=1 ps, at a peak temperature of a few thousand degrees Kelvin; the spike has a lifetime of about 100 picoseconds. During this time the fraction of molecules decomposed can be calculated, using the temperature distribution and a first-order rate equation to solve for the decomposition cross-section. When compared with experiment, the actual values of deposition yield (or atoms of metal deposited per incident ion) are found to be larger than both of the thermal spike predictions by about a factor of two, with the yields of heavier ions (like Xe^+ and Kr^+) predicted more accurately than those of lighter ions (like He^+ and Ne^+).

The second theory is based on the binary collision model for ion-solid interactions, which makes use of the Monte Carlo ion implantation simulation program TRIM.[24, 25] This program is a means of simulating the effects of energetic ions on a material, providing statistics such as mean penetration range, sputtering yield, and point defects produced as a result of ion bombardment. It traces the energy and position of an energetic ion as it transfers energy to the target material atoms through both nuclear and electronic interactions, and assumes that only two bodies

are involved in each collision (the binary collision assumption), and that the material is amorphous. This last assumption means the program is well suited to predict energetic ion effects in polycrystalline materials with randomly oriented grains and neglects ion channelling effects. The model for FIB induced deposition centers on the collision cascade created by an incoming ion and the number of excited surface atoms (ESAs) created in the vicinity of this cascade as a result of knock-on collisions within the material initiated by the ion. Since the metal-bearing gas is adsorbed on the surface, any ESAs beneath them have a finite probability of causing dissociation and causing a metal atom to deposit. The TRIM program is used to determine the distribution of ESAs versus energy, and it is found that number of sputtered atoms as a function of energy $N(E)$ follows a $1/E^2$ dependence. In addition, the probability of dissociation when an ESA collides with an adsorbed gas molecule was calculated, specifically by evaluating the probability of an ESA striking the different atomic species comprising the molecule, and then summing up these separate probabilities into a total fraction function $f(E)$. It is possible to determine the deposition yield Y_D from the expression

$$Y_D = \int_0^\infty f(E)N(E)dE \tag{1.7}$$

where the integration is from zero energy to infinite energy in principle. In actuality, it is sufficient to calculate the integral from $E = 0.1$ eV to $E = 100$ eV. The results of this binary collision model fit the experimental data quite well, although the predictions are somewhat small for the heavier mass ions. This may be because the binary collision approximation may no longer be appropriate for ions as massive as Xe^+ and Kr^+. This model was found through statistical analysis to better match experimental results and is therefore taken to be a better representation of the actual physical phenomenon in question than the thermal spike model, although it is possible that a slightly more sophisticated version of the spike model might provide a better fit to the experimental data. The result of these investigations is the determination that the focused ion beam induced deposition process is substrate-mediated, rather than due to direct interaction of the ion beam with the adsorbed molecules on the surface

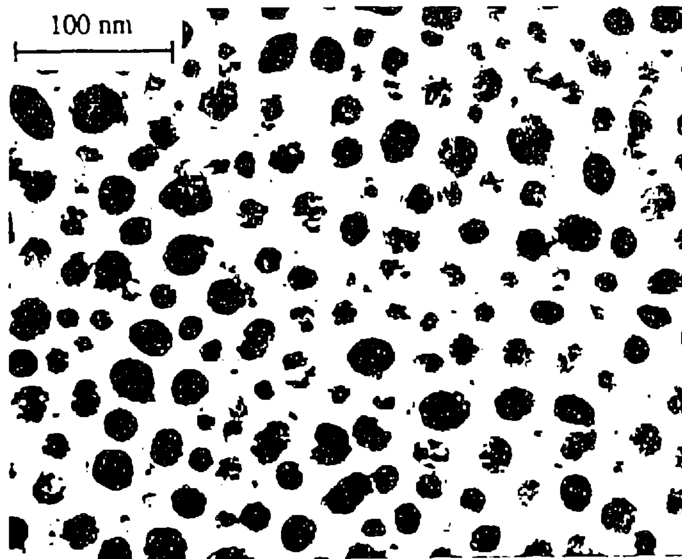

Figure 1-7: Plan view of gold films deposited from DMG(hfac) using 40 kV Ga+ FIB (ref. 28)

or in the gas phase.

As indicated above, one well-studied FIB deposited materials system is gold. The microstructure, resistivity, growth rate, and purity of the films have been investigated as a function of deposition temperature, time averaged current ion current density (the ion beam current divided by the area over which the beam is rastered), and pressure of precursor gas. [26, 27] Through TEM analysis of the films, the microstructure was found to become more coarse as the deposition temperature was increased, and the relative ratio of gold to other impurities (mainly carbon) increased, resulting in films with the resistivity of nearly pure gold (2.44 $\mu\Omega-cm$) at deposition temperatures near 120°C. Similarly, films deposited at higher current densities also showed coarsening and an increase in gold content. The use of high gas pressures during deposition, on the other hand, tended to increase the impurity content of the film. In all cases, the microstructure appeared to consist of islands of gold embedded in a mostly carbon matrix. In the high carbon content films, the gold islands were found to be relatively

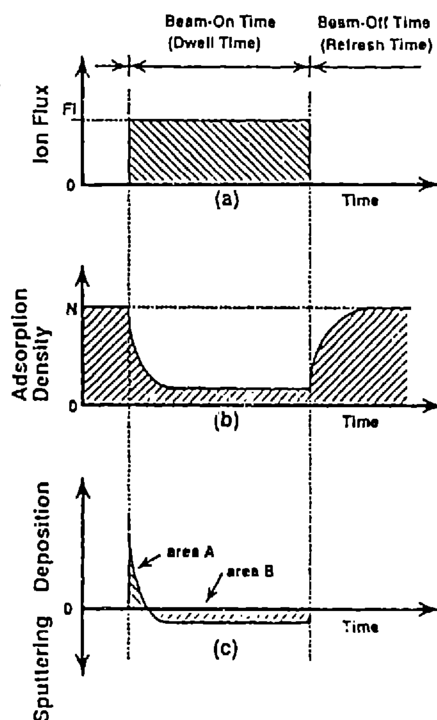

Figure 1-8: (a) Ion flux, (b) gas adsorbate density, and (c) deposition and sputtering as a function of time (ref. 29)

small (figure 1-7), whereas in the films containing a higher percentage of gold the islands were found to be larger and tended to impinge on one another. In cross-section, the films deposited at low temperatures appeared to be discontinuous and partially columnar, at thicknesses up to 0.25 μm.[28] A maximum yield of approximately 10 atoms/ion is obtained at low current densities (4 μA/cm^2), and drops to near zero at a current density of 1 mA/cm^2. The highest growth rate obtainable was about 12 angtroms per second at a current density near 250 μA/cm^2. The organometallic DMG(hfac) appears to be a promising candidate for use as a precursor of focused ion beam induced deposition of gold for the repair of X-ray masks.

One rather important aspect of focused ion beam induced deposition is the scanning rate or dwell time effect. The ion beam dwell time τ_d is defined as the length of time any point on the sample is irradiated by an ion flux. It is expressed simply by $\tau_d = d/v_{scan}$, where d is the diameter of the beam, and v_{scan} is the scanning velocity of the beam. The refresh time τ_r is simply the time between ion pulses for any particular

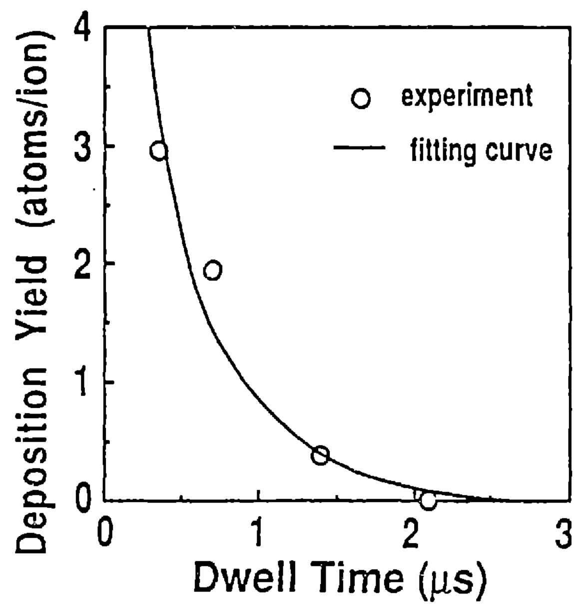

Figure 1-9: Results of a yield vs. dwell time experiment using 30 kV Ga^+ ions at a current density of 8.6 A/cm^2 to dissociate $W(CO)_6$ gas molecules. (ref. 29)

point on the sample, and the loop time is simply the sum of τ_d and τ_r. Focused ion beam induced deposition relies on the presence of an adsorbed precursor gas layer on the substrate, and if the beam dwells long enough on any particular point, the gas layer will be either completely reacted or desorbed and the process of sputtering will overtake that of deposition. This problem is treated mathematically as follows. If one considers the different elements contributing to the rate of gas molecule adsorption on the surface, one arrives at the following expression for the change in n, or the density of adsorbed molecules, with time:[29]

$$\frac{dn}{dt} = cF_g(1 - \frac{n}{N}) - \frac{n}{\tau} - r\sigma F_i n - (1 - r)\sigma F_i n \tag{1.8}$$

where F_g is the organometallic gas flux at the substrate surface, c is the sticking coefficient, N is the density of a complete monolayer of adsorbed gas, τ is the spontaneous desorption lifetime of a gas molecule, r is the fraction of molecules which dissociate, σ is the cross-section for both reaction and desorption, and F_i is the ion flux. The rate of deposition is then given by

$$\frac{dD}{dt} = sr\sigma F_i n - F_i(1 - \frac{n}{N})Y_s \tag{1.9}$$

where s is the number of atoms deposited per dissociation event (ideally one) and Y_s is the sputter yield, or atoms removed per incident ion. Solving these equations results in a complex expression which is most meaningfully studied in graphical form (figure 1-8). The ion flux history experienced by a particular point on the sample is given by figure 1-8(a), and the adsorbate density as a function of time is seen to deplete and recover in an exponential fashion in figure 1-8(b) with the beam on and off, respectively. It can be seen in figure 1-8(c) that in order to cause net deposition, τ_d must be shorter than some critical value, determined by F_g and F_i. When applied to actual experiments, the theory developed here fits the empirical data well. Figure 1-9 shows the results of a low and high current density experiment and the theoretical fit. Note that the low current density deposition yield drops to zero long after the high current density yield, which is to be expected from the model. In addition, it was

determined that decreasing the dwell time or, equivalently, increasing the scanning rate was much more effective in increasing the deposition yield than increasing the flow of organometallic to the sample.

1.3 Objectives

This research reported here is concerned with the issues of the last section, specifically, focused ion beam induced deposition and the effects of the deposition parameters on the resultant film properties and microstructure. The deposited material is copper metal, and the organometallic precursor compound is known in abbreviated form as Cu(hfac)TMVS. The details of this compound and its chemistry will be outlined further in the next chapter on equipment and materials. The basic objectives of this research are:

1. To assess the feasibility of the focused ion beam induced deposition of copper.
2. To measure the yield (in atoms/ion) and growth rate of the deposition under various deposition conditions.
3. To determine the purity and resistivity of the deposited films under various deposition conditions.
4. To evaluate the microstructure of the films as a function of the deposition conditions.

The deposition parameters which are investigated are the temperature of the sample during deposition, T; the time-averaged ion current density, $< J >$; the pressure of organometallic precursor at the sample during deposition, P_{OM}; and the ion beam dwell time, τ_d. The means by which these parameters were varied while the deposition was carried out is the subject of Chapter 3.

1.4 Summary

This chapter gave a brief overview of photolithography, which is the conventional means for submicron interconnect patterning on integrated circuits, and a more detailed look at the newer patterning methods of focused ion beam induced deposition (FIBID) and lithography. The two most important models of FIBID, the thermal spike and binary collision models, were discussed, and the importance of the gas flux and ion beam dwell time was emphasized. Finally, the objectives of this work were enumerated for the reader.

Chapter 2

Equipment and Materials

This chapter will outline the experimental equipment and materials used for the investigation of the focused ion beam induced deposition of copper. The focused ion beam apparatus itself is described, along with the copper organometallic precursor compound and its chemistry. Some attention is also given to the analysis techniques of scanning electron microscopy, transmission electron microscopy, and Auger Electron Spectroscopy.

2.1 Focused Ion Beam

One of the FIB machines used for these experiments is a 50 kilovolt focused ion beam column made by IBT Dubilier Scientific. A schematic diagram of the first system appears in figure 2-1. The column uses a gallium liquid metal ion source from FEI Company and is capable of producing beams as narrow as 70 nm in diameter at low (approximately 25 pA) currents. The beam passes through two lenses and undergoes one crossover, and the position of the crossover with respect to a movable aperture determines the beam current on the sample; this is adjusted by changing the potential on the first, uppermost lens. The size of the beam spot is controlled by the voltage on the second, lower einzel lens. The work chamber is differentially pumped from the column, and the two are separated by a 2 mm aperture, allowing low pressures to be maintained in the column as required to maximize the lifetime

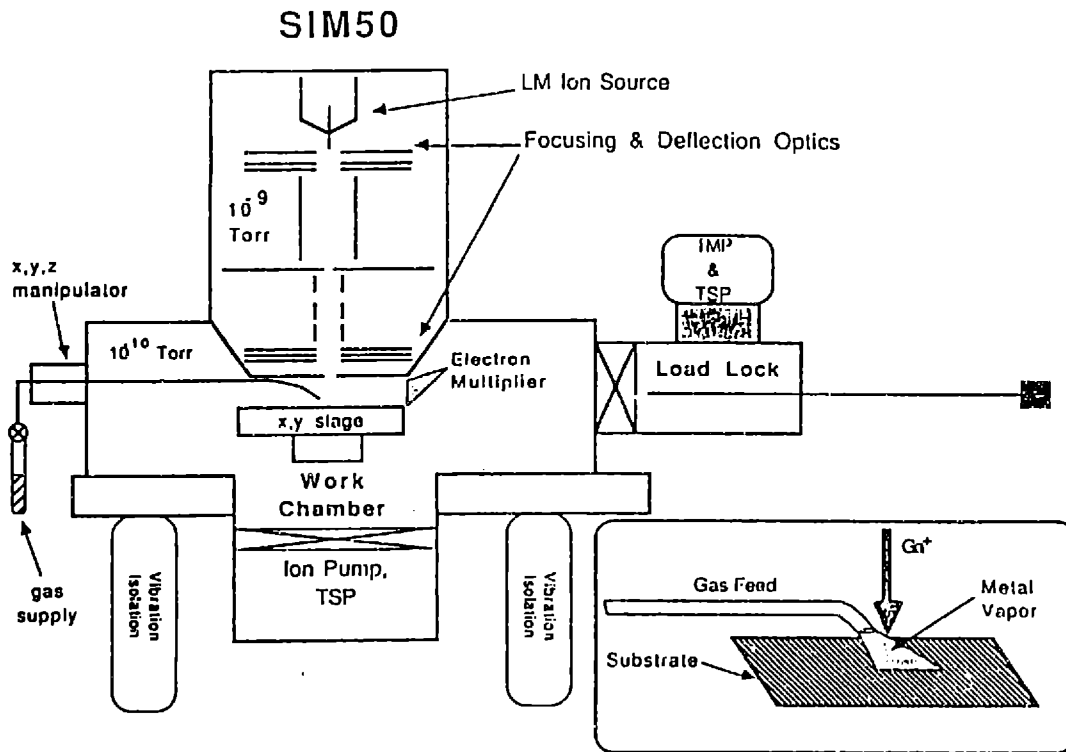

Figure 2-1: The IBT Dubilier Focused Ion Beam system, with custom made work chamber. (ref. 27)

of the source when gases are introduced into the work chamber. The column and work chambers are pumped by separate ion pumps and can achieve pressures in the 10^{-9} torr range. The working distance from the bottom of the differential pumping aperture to the sample is approximately 20 mm. The precursor gas is introduced to the work chamber via a tube fit with a 0.8 mm inner diameter capillary, as seen in the figure. This provides a means of directing the gas flow to the point of ion incidence on the sample; a millitorr ambient of the precursor can be developed immediately around the stage. The height of the capillary tube above the sample determines the pressure at the ion affected zone. During the actual deposition, the gate valve between the load lock and work chamber was left open, and the work chamber ion pump was sealed off, so that only the load lock turbomolecular pump and roughing pump were utilized. The pressure measured at the end of the load lock via a cold cathode pressure gauge while the gas was flowing from the indicated that the overall pressure did not rise above approximately 3 X 10^{-6} torr. The beam scanning system

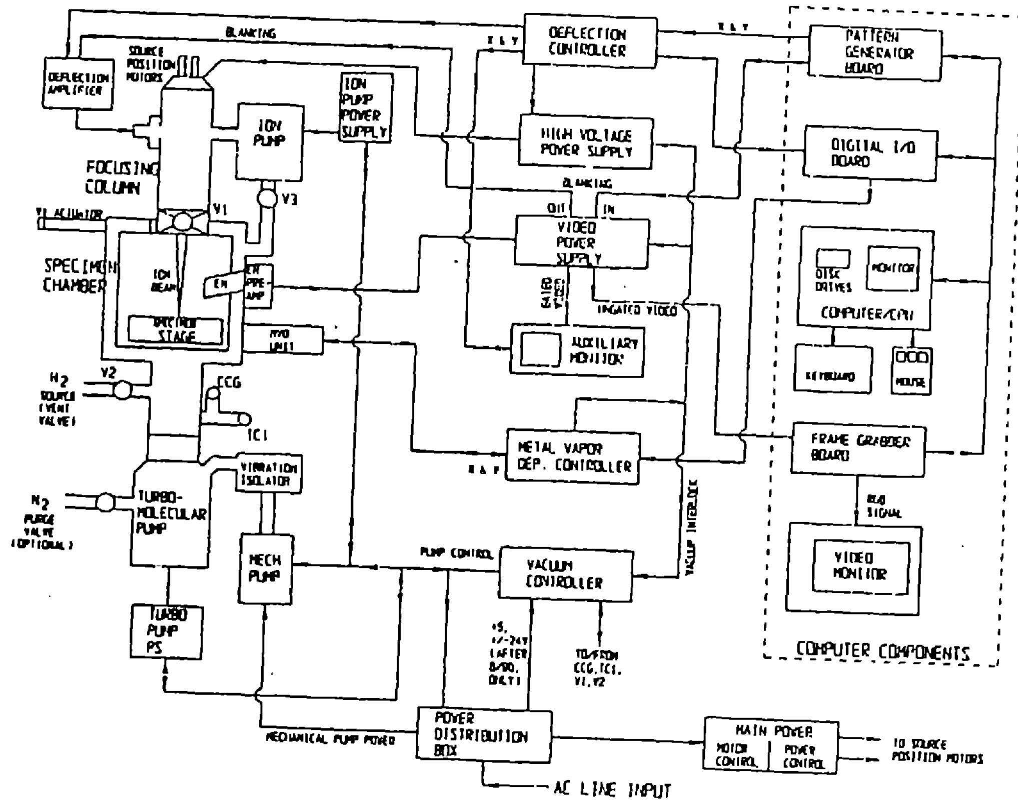

Figure 2-2: The FEI FIB 500D Focused Ion Beam Milli‿g System (FEI Company)

consists of a signal generator to develop the ramp voltages and a pulse amplifier. The system is only capable of writing lines and boxes since a means of electrostatically diverting or blanking the beam from the sample to halt milling or deposition is not currently possible on this apparatus. This simple patterning capability, however, was adequate for the studies carried out in this project. The stage can be moved in the X and Y (horizontal plane) directions using high vacuum stepper motors from Princeton Research. Another limitation of this apparatus is that it is not possible to tilt the sample or change the working distance once the sample is in place in the work chamber, although this also did not present any major difficulties. Imaging in this system is accomplished by detecting secondary electrons generated by the ions with a channel electron multiplier (CEM). This intensity signal from the CEM was fed into the Z input of a Leader cathode ray tube display, while the X and Y inputs were the X and Y ramp voltages from the signal generator. In this way, a video image similar to that obtainable from a scanning electron microscope could be produced.

The other FIB system used in these experiments is a 25 kilovolt FIB 500D focused

ion beam milling system manufactured by FEI Company, shown in figure 2-2. This machine operates on the same basic principle as the Dubilier column, except that the work chamber in the former typically can only achieve an ultimate pressure of close to 1 X 10^{-7} torr, since the 500D lacks a load lock and must be vented to atmosphere during each sample change. The scanning system is somewhat more sophisticated than that developed for the Dubilier column and offers beam blanking, automatic timing of depositions and milling, and the ability to independently adjust the beam dwell time and scanning area. The ions are focused by two lenses with a movable aperture, but the beam does not undergo a crossover in its path from the source to the sample stage. The size and current of the beam is determined by the size of the variable aperture interposed between the source and stage; the smallest spot size obtainable on this machine is between 50 and 100 nm, with a beam current on the order of tens of picoamperes. Note that like the IBT Dubilier machine, the ultimate beam size is somewhat large compared to beams on the order of tens of angstroms available from high voltage focused ion beams. The maximum useful magnification of this system is about 20,000x, depending on the beam size. There is also a means of capturing images in digitized form and storing them on disk for future recall. This machine has the advantage of a fully tiltable stage and a Z height control for the stage to adjust the working distance to the sample.

For both machines, Cu(hfac)TMVS precursor gas is fed into the chamber and directed to the stage via a capillary tube similar to the one in the Dubilier machine. A schematic diagram of the gas manifold used to deliver the precursor is shown in figure 2-3. The vapor pressure of the copper compound is low enough so that the gas flow need only be regulated with a needle valve. The pressure attained at the sample for the copper precursor compound used in these experiments depends on the distance of the capillary tube from the sample surface and has been measured. The maximum pressure, obtained when the capillary tube is touching the sample surface, is about 3 mtorr.

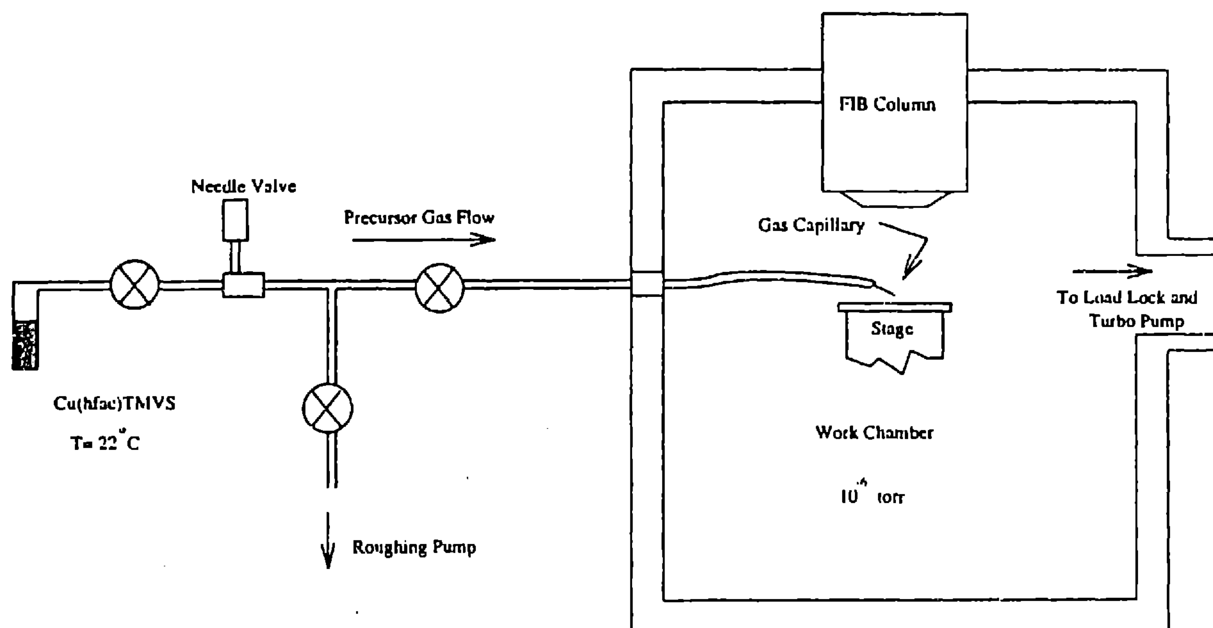

Figure 2-3: Gas manifold for introduction of Cu(hfac)TMVS precursor into the work chamber.

2.2 Copper Precursor

The chemistry of the organometallic precursor deserves some mention at this point. The technical name for the compound used is copper(+1) hexafluoroacetylacetonate trimethylvinylsilane, abbreviated Cu(hfac)TMVS, and the molecule is illustrated in figure 2-4(a).[30] The TMVS group stabilizes the Cu^{+1} oxidation state at room temperature, but breaks off as temperatures exceed about 120°C. This compound is a straw-yellow or greenish-yellow, low viscosity liquid, with vapor pressure characteristics as indicated in figure 2-4(b). The precursor requires little or no heating to provide a sufficient vapor pressure for the experiments carried out in this thesis. The main use of this compound to date has been in selective copper organometallic chemical vapor deposition (OMCVD), in which vapors of Cu(hfac)TMVS are passed over a heated sample. At high temperatures, the TMVS group detaches from the Cu^{+1}, exposing

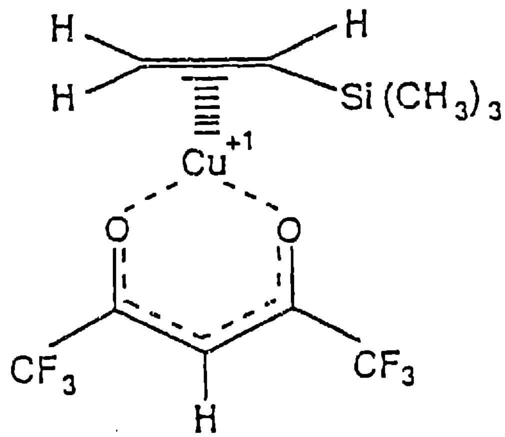

(a)

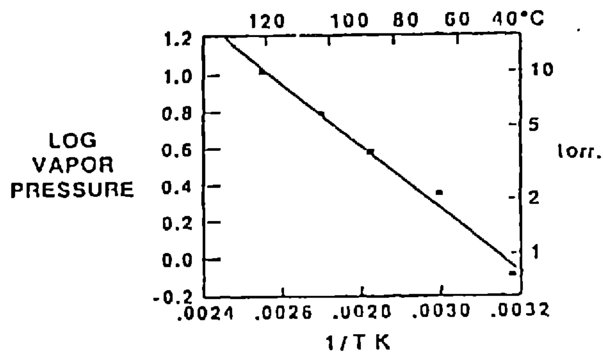

(b)

Figure 2-4: (a) Copper(+1) hexafluoroacetylacetonate trimethylvinylsilane, a.k.a. Cu(hfac)TMVS, and (b) vapor pressure characteristics (ref. 30,31)

this reactive ion. The resulting chemical reaction ensues:

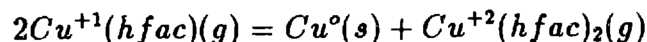

$$2Cu^{+1}(hfac)(g) = Cu^{o}(s) + Cu^{+2}(hfac)_2(g)$$

and the TMVS groups and $Cu^{+2}(hfac)_2$ byproducts are carried away. In OMCVD, this reaction is very clean because the products are gaseous and no reagents are required to assist the deposition, resulting in pure copper deposition. The distinctive feature of this compound is the electron transfer that occurs between the exposed copper ions. This transfer occurs far more readily on conductors than on insulators, and highly selective copper deposition has been demonstrated on a variety of conducting substrates. In these experiments, thin lines of conductors were embedded in oxide trenches, so that alternating strips of metal and insulator were exposed to the gas flow at temperatures exceeding 120°C. In all cases, the copper metal selectively deposited on the conductor rather than the oxide.[31] One must be certain, however, that the SiO_2 used is completely free of adsorbed water vapor, as any H_2O present will act as a seed for copper growth. For this reason, much better selectivity is typically achieved with the dense thermal oxides typically used for microelectronics purposes than with less dense, porous SiO_2 substrates, which tend to trap water vapor. One other interesting aspect of this compound concerns its potential use as a copper etchant. If the reaction mentioned above is run in reverse, copper metal can be removed from the solid to the gaseous phase as Cu(hfac)TMVS. When the TMVS and $Cu(hfac)_2$ byproducts were passed over a copper metal sample at elevated temperatures in these etching experiments, a substantial portion of the copper was found to be removed through the reverse reaction. [31]

2.3 Auger Electron Spectroscopy (AES)

This analytical technique is extremely useful for determining the composition of samples, and was used in this thesis to determine the relative fractions of copper and carbon byproducts in the deposited films. The typical equipment is a high vacuum

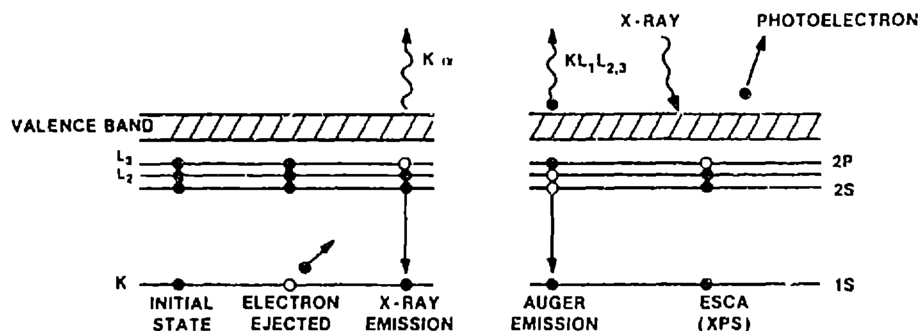

Figure 2-5: Types of transitions occurring in electron shells when struck by an energetic electron. (ref. 32)

chamber fitted with an electron beam column similar to that used in scanning electron microscopy. An argon ion sputtering gun is also a standard part of the AES apparatus. Using an electron beam on the order of 0.05 μm, it is possible to selectively probe areas for the presence of various elements and their relative amounts. The transitions which occur in the electron shells when subjected to a high energy electron beam or incident radiation are illustrated in figure 2-5. Typically, X-rays, secondary electrons, photoelectrons, and Auger electrons are emitted, and the latter situation is particularly important to AES. The kinetic energy of the transition from, for instance, the L shell to the K shell is borne by the Auger electron in this case instead of a photon. Since these transitions are unique for each element, the detection of secondary electrons with a particular energy uniquely identifies that element in the sample, although a detailed knowledge of the energy transitions characteristic of each element is necessary to avoid confusion. Typically, when Auger spectra are taken, the data is viewed in derivative form; that is, the plot of electron counts versus

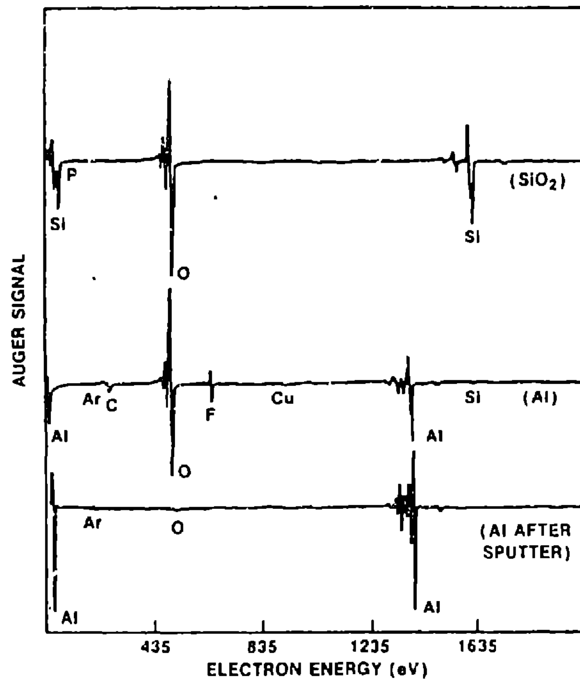

Figure 2-6: Auger Electron Spectroscopic data displayed in derivative form. (ref. 32)

kinetic energy of the electron is differentiated with respect to energy to produce a graph like that shown in figure 2-6. This makes the presence of electrons at a particular energy obvious and aids in the identification of elements present in small atomic concentrations in the sample. It is also usually possible to sputter or mill away layers of the sample with a plasma of some inert gas such as argon, and thus remove any residual contamination on the surface or to determine the concentrations of various elements as a function of depth. The technique actually probes only a very small thickness at the surface, up to about ten atomic layers depending on the beam energy, so that sputtering is necessary when attempting cross-sections of structures like silicide layers and contacts. Typically a calibration standard similar to the specimen being investigated is required to obtain a highly quantitative composition analysis, but it is possible to obtain a rough idea of the main chemical components without such a standard. [32, 33]

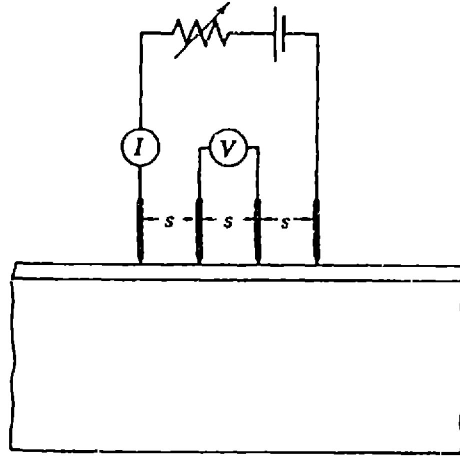

Figure 2-7: Four point probe measurement for resistivity determination. (ref. 34)

2.4 Resistivity Measurements

The resistivity ρ of a material is defined simply in the following manner:

$$\rho = \frac{V}{I}\frac{A}{l} = R\frac{A}{l} \tag{2.1}$$

where V is voltage, I is current, R is resistance, l is the length of the sample, and A is the cross-sectional area. The resistivity (often measured in Ω-cm or $\mu\Omega$-cm) of the deposited copper in this thesis was measured using a four-point probe apparatus, diagrammed schematically in figure 2-7. A Hewlett Packard voltmeter and current source were used in the actual apparatus. In this type of measurement, a fixed current is established between the outer two points on the test pattern or sample, and the voltage betweeen two points separated by a distance l is measured. The resistance of the voltmeter is typically much greater than that of the sample; very little current is drawn by the voltmeter during the measurement as a result, so the true voltage can be

determined according to equation 2.1 and hence an accurate resistivity measurement of the sample can be made.

2.5 Profilometry

The method used to measure the thicknesses of depositions was profilometry, specifically using a Tencor Alpha Step 200 Profilometer. A stylus with a mass of a few grams is traced across a sample at a velocity of several to a few tens of microns per second; the motion of the stylus is detected by a transducer, and a plot of stylus deflection normal to the sample surface versus distance traversed parallel to the surface is typically obtained. This instrument is typically sensitive to thickness variations on the order of 5 nm μm or so, and has sufficient resolution for the measurements required in these experiments.

2.6 Scanning Electron Microscopy

This instrument is similar to the Auger instrument discussed above in that it uses a relatively low voltage electron beam focused to submicron dimensions, and a schematic of a standard SEM appears in figure 2-8. Its primary function is to image samples by detecting the secondary electron emission induced by incident electrons, in much the same manner as samples are imaged in the FIB. Typical secondary electron detection methods include channel electron multipliers and scintillation counters. This technique was applied to view the copper depositions made in this thesis to examine the surface texture. It is very surface specific, since the secondary electrons are originated only within escape depth of the surface, which is about 10-50 angstroms. Because of this, sloping edges tend to appear brighter than flat regions, since in the former case more of the interaction volume of the electron is within escape distance of the surface. It is also possible for backscattered electrons to produce secondary electrons at some distance from the point of electron incidence. These backscattered electrons typically return to the detector at energies very close to the incident ion energies,

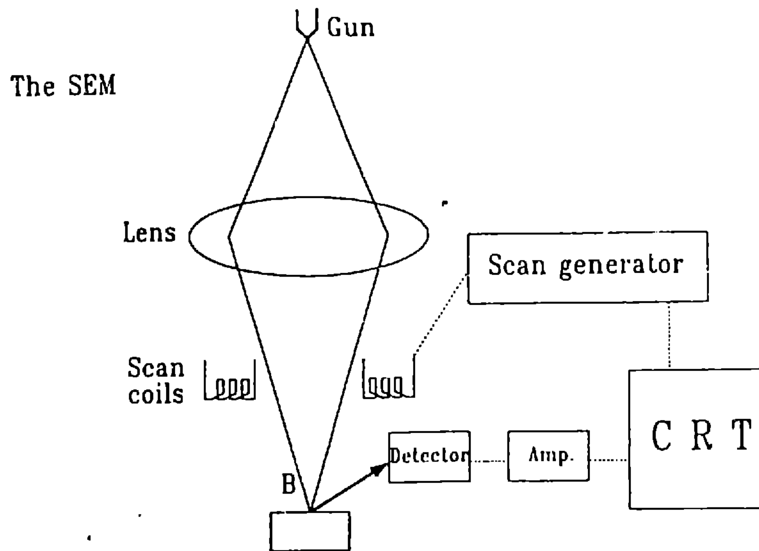

Figure 2-8: Block diagram of the lens and detector system in a scanning electron microscope. (ref. 35)

and can provide atomic species information about the sample. High atomic number (Z) materials appear brighter than low Z materials, but again, these electrons can only be detected near the surface and not very far into the bulk of the material. To see Z contrast and crystallographic information from the bulk, transmission electron microscopy (TEM) is the technique of choice.[35, 36]

2.7 Transmission Electron Microscopy

The transmission electron microscope (TEM) used in investigating these copper depositions was a JEOL 200CX. Typical acceleration voltages are on the order of 200 kV to achieve transmission of the electron beam through the approximately 0.2 μm sample thickness. A diagram of this instrument appears in figure 2-9.

In its normal imaging mode of operation, the electron beam is focused with magnetic lenses and an image is obtained in a manner analogous to light in an optical

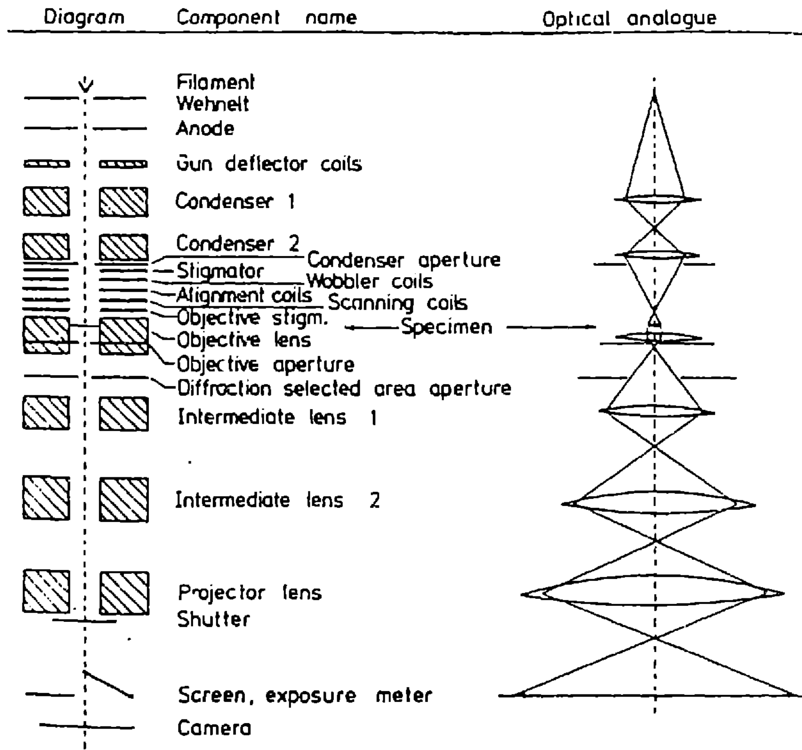

Figure 2-9: Diagram of a typical transmission electron microscope (TEM) and optical analogue. (ref. 35)

microscope. It is possible to obtain magnifications of several hundred thousand times, much higher than that achievable in a scanning electron microscope. The images, like those from the SEM, can be easily interpreted.

One of the most important features of the TEM is its ability to provide crystallographic information on the sample using electron diffraction. The simple Bragg condition for diffraction

$$2d(hkl)\sin\theta = n\lambda \tag{2.2}$$

where $d(hkl)$ is the spacing between planes sharing the Miller indices (hkl), θ is the angle between the incident beam and the (hkl) plane, and λ is the wavelength of the electrons given by the DeBroglie relation. All planes with these indices will diffract the electron beam. If the sample is polycrystalline, the resultant image will appear to be a series of sharp concentric rings composed of individual spots; the ring structure is the result of a distribution of grain orientations within the plane of the film. Similarly, an amorphous film will give a series of diffuse rings arising from the distribution of interatomic distances present in this type of structure. It is also possible in this instrument to carry out dark field microscopy, which involves introducing an aperture to select only a single diffracted beam, corresponding to a particular crystallographic orientation. As a result, when viewed in imaging mode, those particular grains or crystallites with the particular orientation selected will appear brighter than the surroundings. The TEM was used in these experiments to make plan-view (viewed normal to the plane of the film) examinations of the microstructure of the copper film depositions. [35, 36]

2.8 Summary

In this chapter, the focused ion beam equipment used in these experiments were described. An outline of the properties and chemistry of the copper precursor compound, Cu(hfac)TMVS, for selective organometallic CVD was presented. Finally, the characterization techniques of Auger Electron Spectroscopy, four point probe measurements, profilometry, scanning electron microscopy, and transmission electron

microscopy were all described.

Chapter 3

Experimental Procedures

3.1 Yield Experiments

One of the characteristics of the copper depositions initially investigated was the deposition yield, or number of atoms deposited per incident gallium ion. For these initial experiments, the yield was calculated assuming the atomic density of pure copper, and only later was this figure adjusted for the high impurity content (mostly carbon) after determining the film composition using Auger Electron Spectroscopy.

3.1.1 General Deposition Procedure

The depositions were carried out on both silicon substrates and 100 nm thermal SiO_2 on silicon substrates. During depositions, the ion pump at the bottom of the work chamber of the UHV system was closed off; the chamber was pumped solely by the load lock turbomolecular pump. The ultimate pressure reached in the chamber in this manner before the precursor gas was introduced for deposition was on the order of 1×10^{-7} torr. The gas manifold was pumped with a roughing pump to below 100 mtorr, closed off to the mechanical pump, and then opened to the turbo-pumped work chamber, causing a rise in pressure here as the gas manifold was pumped through the 0.8 mm inner diameter capillary tube. After several hours, the work chamber pressure would recover to its initial low value and deposition could proceed.

The actual deposition procedure began by location of the point on the sample desired and maneuvering of the capillary tube to direct the gas flow to that area. This could all be done fairly easily by viewing the secondary electron image of the sample and tube on the video monitor. For most of the yield experiments, the capillary was positioned 200 microns above the substrate and 50 microns laterally from the point of ion incidence; the yield experiments for the investigation of gas pressure effects, however, involved depositing with the capillary tube between 0 and 2 mm above the substrate. Contact of the capillary tube with the sample could be detected by noting the abrupt cessation of vibration in the tube on the video screen, and the tube could be raised via a micrometer to a known height in the direction perpendicular to the sample surface.

Before deposition, a valve on the manifold separating the Cu(hfac)TMVS ampoule from the rest of the vacuum system was opened. This typically caused the pressure, as read via a cold cathode gauge far away from the point of gas introduction, to rise to about 1 X 10^{-6} torr from the base pressure. Some short period of time was required to allow the pressure to stabilize. To initiate the deposition, the scanning area of the beam was confined to either a line 300 μm in length by connecting the two X deflection plates to ground, or by increasing the magnification such that the beam scanned a square of 10 or 20 μm on a side. The ions were accelerated by a potential of 35 kilovolts. The deposition was halted by scanning the beam over a much larger area and effectively reducing the deposition rate to zero. Some small amount of deposition probably occurred for a short period before and after the deposition while the beam scanned a large (300 μm on a side) area, but this is for all purposes negligible; the average current density during these periods was very low and these periods were short compared to the actual deposition times of 10 to 20 minutes.

3.1.2 Current Density Dependence

For the investigation of yield as a function of average current density, depositions were made onto a fixed area using different beam currents. As noted before, the beam current could be altered by changing the Lens 1 voltage and hence the position

of the beam crossover in the movable aperture in the IBT Dubilier FIB. The actual beam current could be measured using a Faraday cup on the stage beneath a nickel mesh; the beam was directed through one of the holes in the mesh (of 25 μm period) and current could be measured as the beam struck the bottom of the cup. In this way it was possible to avoid measuring a spurious additional current due to secondary electron emission.

3.1.3 Gas Pressure Dependence

For the investigation of yield versus gas pressure, the depositions were carried out in the general method outlined above except that the capillary tube was held a different distance above the sample for each run. The tube was held 50 μm horizontally from the site of ion bombardment and between 0 and 1.25 mm vertically above the sample. In this manner, the local gas pressure at the point of deposition could be varied. A later section details the process by which the gas pressure as a function of capillary tube height was measured at the site of deposition. Once this information was obtained then the dependence of deposition yield on local gas pressure at the sample was known.

3.1.4 Dwell Time Dependence

In determining the dependence of the yield on the dwell time, the capillary tube was set at a fixed height of 200 μm above the sample and 50 μm laterally away from the deposition point. The beam current was maintained at a constant value through a constant Lens 1 value on the IBT Dubilier FIB. The beam was scanned along a 300 μm long path in the Y direction while grounding the X electrostatic deflection plates. The scanning frequency in the Y direction was varied by changing the frequency on the signal generator. A frequency range from several tens of Hertz to over 10^4 Hertz could be covered in this manner, which amounted to a range of dwell times from 10 ns to several tens of microseconds.

3.1.5 Measurement and Calculation

The thickness of the depositions was measured using a profilometer, and the line widths were measured using SEM. The lines are assumed to have approximately rectangular cross sections, and the yield Y, in atoms/ion, is determined by

$$Y = \frac{t\rho}{C} \tag{3.1}$$

where t is the deposit thickness in cm; ρ is the atomic density of the deposit (atoms/cm^3), assumed to be equal to the pure, bulk value; and C is the ion dose in ions/cm^2. The ion dose is merely the total number of ions implanted per unit area.

3.2 Resistivity

The resistivity is a critical property of the deposited film and was measured as a function of temperature, average current density of deposition, and ion beam dwell time.

3.2.1 Temperature Dependence

The depositions for the measurement of resistivity as a function of temperature were carried out using a resistively heated stage. The temperature during deposition was monitored with a copper-constantan thermocouple in intimate thermal contact with the sample stage. It was possible to heat the stage from room temperature to over 100°C in this way. After stabilization of the temperature reading on the thermocouple gauge, depositions were carried out in the same manner as the general deposition procedure described above, with the capillary tube held 200 μm above the sample surface.

The depositions were carried out upon a specially fabricated tungsten finger pattern, a diagram of which appears in figure 3-1. This pattern was fabricated from 60 nm of electron beam evaporated tungsten on 100 nm thermal SiO_2. During deposition, the sample was positioned so that a 300 μm line could be drawn between the outer

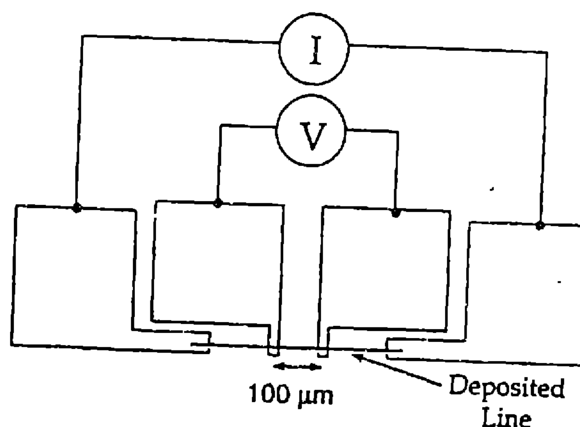

Figure 3-1: Finger pattern used for four point probe resistivity measurements.

two fingers and across the inner two. This greatly facilitated the four point probe measurements, which were then made by passing a fixed current (1 mA) through the outer two bond pads and measuring the voltage between the inner two bond pads.

It must be noted that at high temperatures a significant amount of stage drift is noticed, especially during long depositions (> 10 minutes or so), which causes deposited lines to exhibit widths somewhat larger than the actual beam diameter. This was noticed during high temperature deposition of gold also.[37] It is conjectured that the use of a very localized heating source designed to heat only the ion beam affected area (a laser or highly focused light beam, for instance) would greatly reduce the severity of this problem.

3.2.2 Current Density Dependence

This experiment was carried out in much the same way as the investigation of yield as a function of average current density. In this case, the depositions were performed

on the finger pattern on oxide, with the same capillary tube height as in the general procedure. The current density was varied by varying the beam crossover position in the movable aperture by changing the Lens 1 Voltage in the IBT Dubilier column.

3.2.3 Dwell Time Dependence

This investigation followed the same general deposition procedure as the experiment exploring the yield versus dwell time, except that here lines were written on the finger test pattern. The capillary tube height was maintained at 200 μm above the sample. The dwell time was varied from several tens of nanoseconds to over 10 microseconds by varying the scanning frequency on the signal generator.

3.3 Gas Pressure at the Sample

The gas flow conditions during deposition at the point of ion incidence were simulated through the use of a stagnation tube, and pressure at the point the copper precursor gas was introduced to the chamber was measured via a capacitance manometer. This equipment appears in figure 3-2, which shows the experimental setup for these measurements. The stagnation tube consists of a flat stainless steel piece connected to a stainless steel tube. The flat piece is perforated to allow gas to enter the tube, and simulates the effects on the gas flow of the flat substrate and stage during actual deposition. To measure the gas pressure, the stagnation tube and manifold leading to the capacitance manometer is first pumped down by a roughing pump. It is then opened up to the work chamber for further pumping. The Cu(hfac)TMVS precursor gas is then fed into the chamber via the capillary tube, and the tube is positioned such that it directs gas directly into the hole at the end of the stagnation tube; this is ensured by maximizing the pressure reading obtained on the capacitance manometer. The tube can then be set at various heights as indicated by a micrometer and, after allowing some time for stabilization of the manometer, the local pressure at the

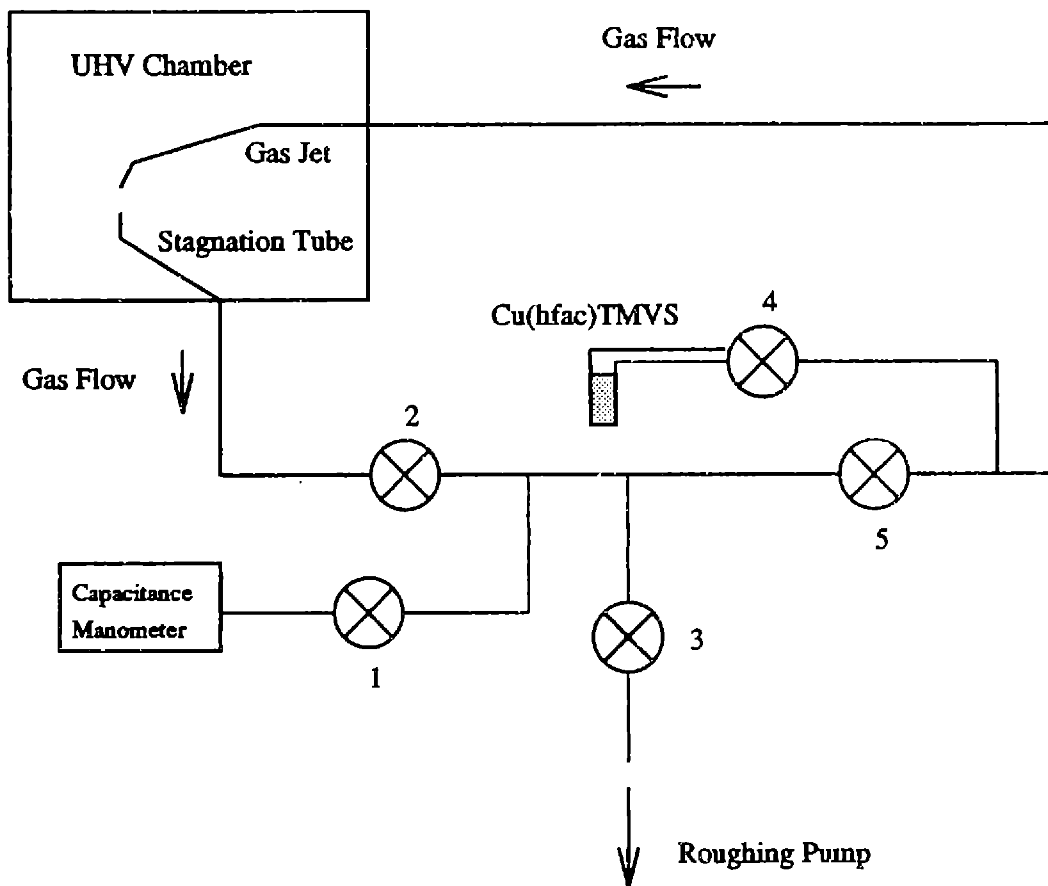

Figure 3-2: Schematic arrangement for stagnation tube experiment to measure local precursor gas pressure. To measure the pressure, valves 1,2, and 4 are left open and valves 3 and 5 are closed.

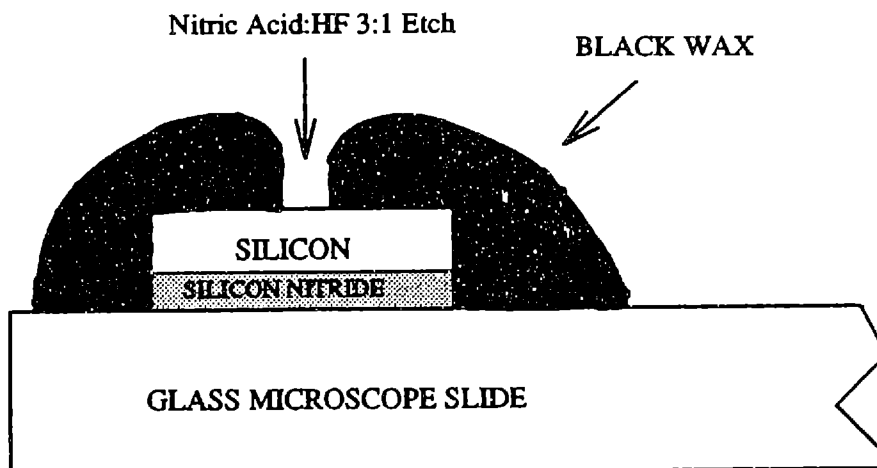

Figure 3-3: Preparation of silicon nitride membranes for TEM.

mouth of the stagnation tube can be obtained. This is a relatively straightforward and accurate means of experimentally determining this important deposition parameter.

3.4 TEM Sample Preparation

The samples were all prepared from a wafer of silicon with a 1000 Angstrom layer of silicon nitride. The wafer was diced into small (3 mm x 3 mm) sections and these pieces were affixed face down on a disc grinder with wax. The sample could then be ground down from the back using 1 μm grain sandpaper to a thickness of approximately 125 μm. The samples were removed from the disc grinder and affixed face down on a glass microscope slide with black wax, as illustrated in figure 3-3, leaving a small hole in the wax near the center of the sample. The slide could then be immersed in a 3:1 volume ratio mixture of nitric acid and hydrofluoric acid, which etched only the part of the sample exposed to the acid. The silicon nitride layer on the front side acted as an etch stop; the sample was found to be thinned sufficiently

once the etched hole became translucent. This indicated the presence of a 0.1 μm thick silicon nitride membrane of approximately 100 to 200 μm diameter which could easily be penetrated by the 200 kV electron beam in the TEM.

Once the membranes were prepared, the focused ion beam induced deposition of a thin film of copper could then be carried out on them. Since the FIB is only capable of depositing rather small areas of film, the sample preparation was greatly facilitated by preparing the membranes first and then depositing on them rather than by writing the film first and then attempting to locate and thin down the exceedingly small (several hundred square microns) deposition area. The TEM samples were deposited in the FEI FIB 500D system at an acceleration voltage of 25 kilovolts by following similar general deposition procedures as in the IBT Dubilier system.

3.5 Auger Electron Spectroscopy

Samples for these measurements were deposited on silicon or silicon dioxide coated silicon wafers in small patches of 10 x 10 or 20 x 20 μm^2. The ion sputtering gun in the AES apparatus was utilized to remove a few tens of angstroms of the surface with a 2 kV, 10 $\mu A/cm^2$ current density argon ion beam until the carbon content was found to be constant with respect to distance into the sample. The readings were made at an electron beam current of 5 to 30 nA using a 3 to 5 kV acceleration potential. For some of the more resistive samples deposited on silicon dioxide, it was necessary to use the lowest beam currents and acceleration potentials in the ranges cited and to employ a 60° stage tilt to minimize sample charging.

3.6 Summary

This chapter outlined the basic experimental procedures followed for deposition of the copper films for yield, growth rate, resistivity, composition, and microstructure investigation. The procedure for determining the local precursor pressure at the substrate using a stagnation tube and capacitance manometer were also described.

In addition, some experimental parameters used during Auger composition analysis were provided.

Chapter 4

Results and Discussion

The results of the analysis of yield, growth rate, resistivity, composition, and microstructure as a function of the principle variables of substrate temperature during deposition; time-averaged current density, or beam current divided by the area scanned; the pressure of the Cu(hfac)TMVS at the sample during deposition; and the ion beam dwell time, are detailed here. The results of the pressure measurements are also presented. The general trends in the data are described and some interpretation of the results is given.

4.1 Local Gas Pressure

The results of the stagnation tube experiments outlined in the previous chapter can be summed up in the graph in figure 4-1. The curve follows the general shape expected for this type of measurement, conforming to the equation for the pressure of organometallic gas P_{OM} at a point D, released from a tube of radius R:

$$P_{OM}(D) = P_{OM}(0)(1 - \frac{1}{\sqrt{1 + (\frac{R}{D})^2}}), \tag{4.1}$$

where $P_{OM}(0)$ is the pressure of the precursor at the mouth of the tube. A maximum pressure of close to 3 mtorr is noted when the mouth of the tube is touching the substrate. For most of these experiments, the capillary was held at a distance of 0.2 mm

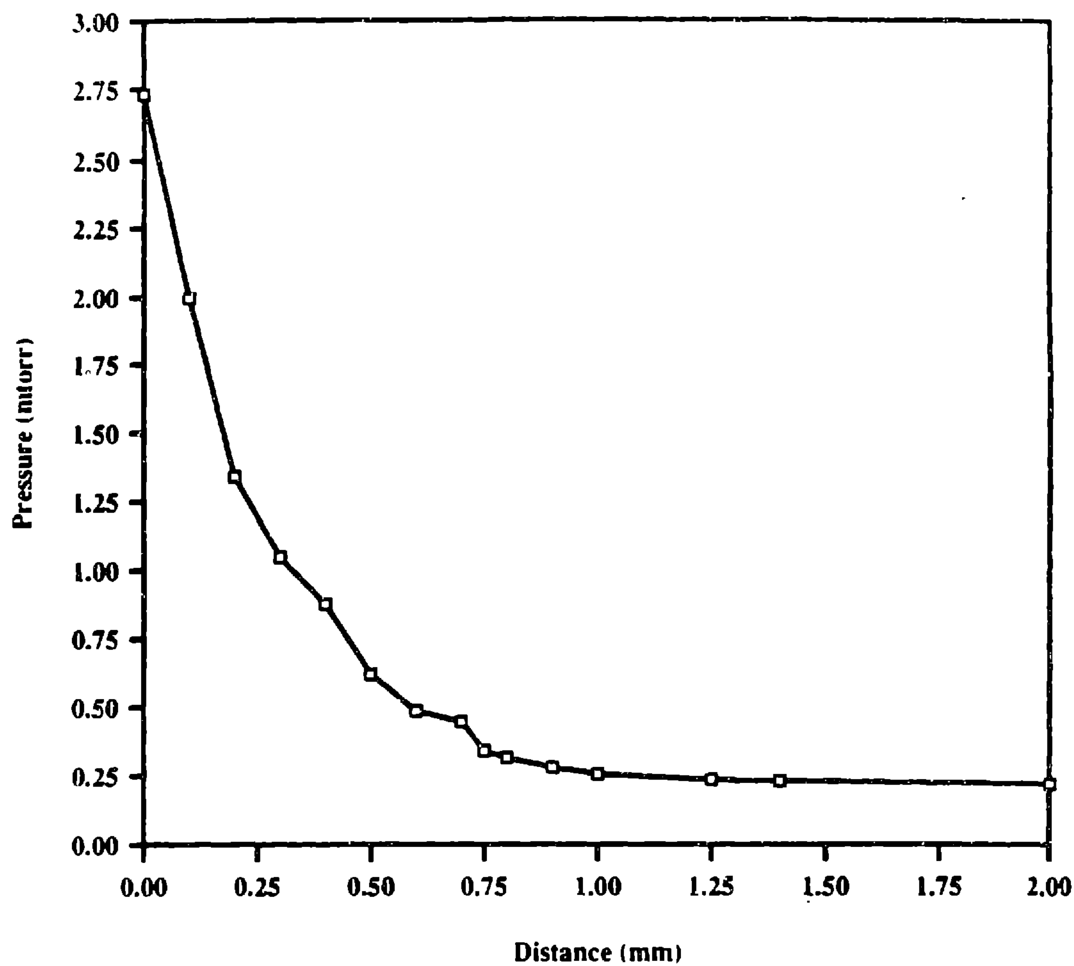

Figure 4-1: Graph of Cu(hfac)TMVS precursor pressure measured as a function of distance from the mouth of the capillary tube via a stagnation tube and capacitance manometer.

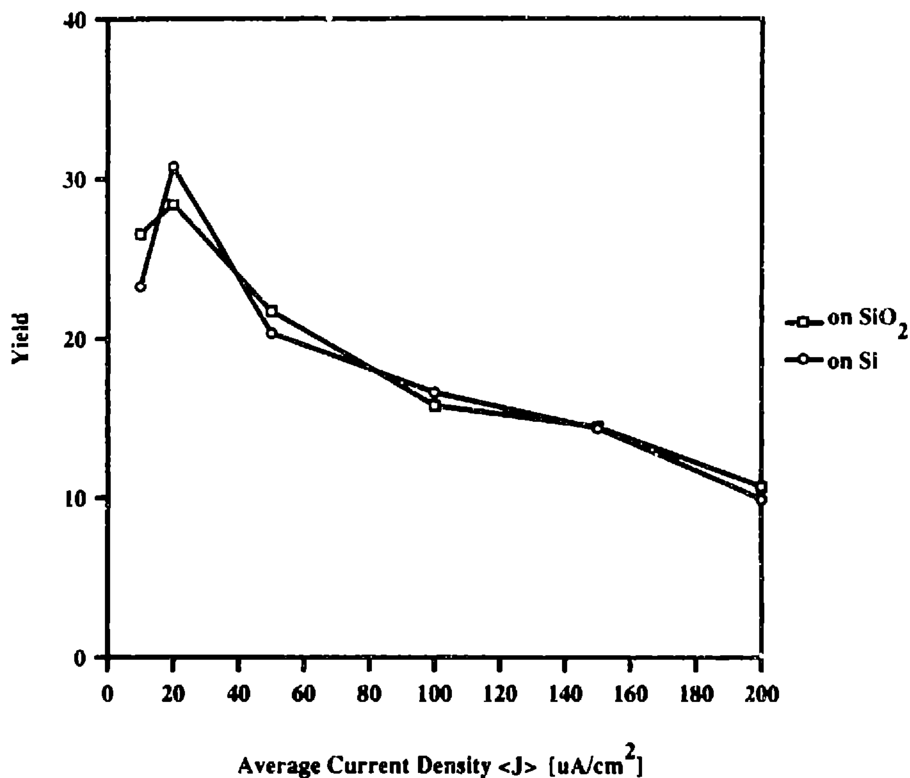

Figure 4-2: Yield data in atoms per incident gallium ion, assuming the film has the density of pure bulk copper, on silicon and silicon dioxide substrates, as a function of average current density of deposition. The films were deposited using 35 keV Ga^+ at room temperature, at an estimated copper precursor pressure of approximately 1.5 mtorr.

from the sample surface, which corresponds to a precursor pressure of approximately 1.5 mtorr. The tube was also held 50 μm laterally from the point of ion incidence, but this small horizontal shift did not change the pressure reading significantly and can be neglected.

4.2 Yield and Growth Rate

4.2.1 Average Current Density Dependence

Yield results appear in figure 4-2 for depositions on both a silicon substrate and a 100 nm SiO_2 layer on silicon, as a function of the average current density during deposition. One should first note that this yield is calculated assuming the film has the atomic density of pure copper, and second, that this is the *net* yield, or the difference

between the decomposition yield and the sputter yield. The first notable aspect of this plot is that the yield is approximately the same regardless of the substrate. This is to be expected in focused ion beam induced deposition, since once the film thickness is more than about a hundred angstroms (the penetration depth of gallium ions at these acceleration potentials in copper metal), the film growth occurs on copper metal and is independent of the underlying substrate. The second important aspect of this type of plot is the shape of the curve. The maximum yield, measured in units of film atoms per incident ion, is approximately 28 at an average deposition current density of 20 $\mu A/cm^2$. The general trend exhibited here is a slight increase in yield to peak at around 20 $\mu A/cm^2$ and then a gradual decrease in yield as the average current density is increased. A minimum value of about 10 film atoms per incident ion is noted at the highest current density of 200 $\mu A/cm^2$.

The curve shape is largely determined by the density of adsorbed molecules on the surface under different ion fluxes. At relatively low ion fluxes, or average current densities, an increase in the ion flux seems to result in a similarly increasing deposition yield. This is the regime in which the gas molecules adsorbed on the sample surface can be readily replenished by the gas molecule flux, which is fixed by the pressure of the precursor gas at the point of ion incidence. As the ion flux exceeds a certain value, the areal density of adsorbed gas molecules is reduced as sputtering of the film atoms by the incident ions becomes significant; hence the net yield is reduced. This effect is similar to the adsorbate depletion effect found at long ion beam dwell times, as discussed in Chapter 1 of this thesis.[29]

The gradual decline in the net yield demonstrates that the gas flux to the sample at this particular gas capillary-to-substrate distance (0.2 mm) is not sufficient to refresh the ion beam desorbed and decomposed gas molecules at time-averaged ion current densities greater than 20 $\mu A/cm^2$. To broaden the regime in which the deposition yield increases or remains constant with increasing ion flux, the gas pressure could be increased by decreasing the capillary tube height. Once the gas molecules have presumably adsorbed in a monolayer, however, the yield will no longer continue to increase, even if the gas pressure is increased further. This effect is investigated

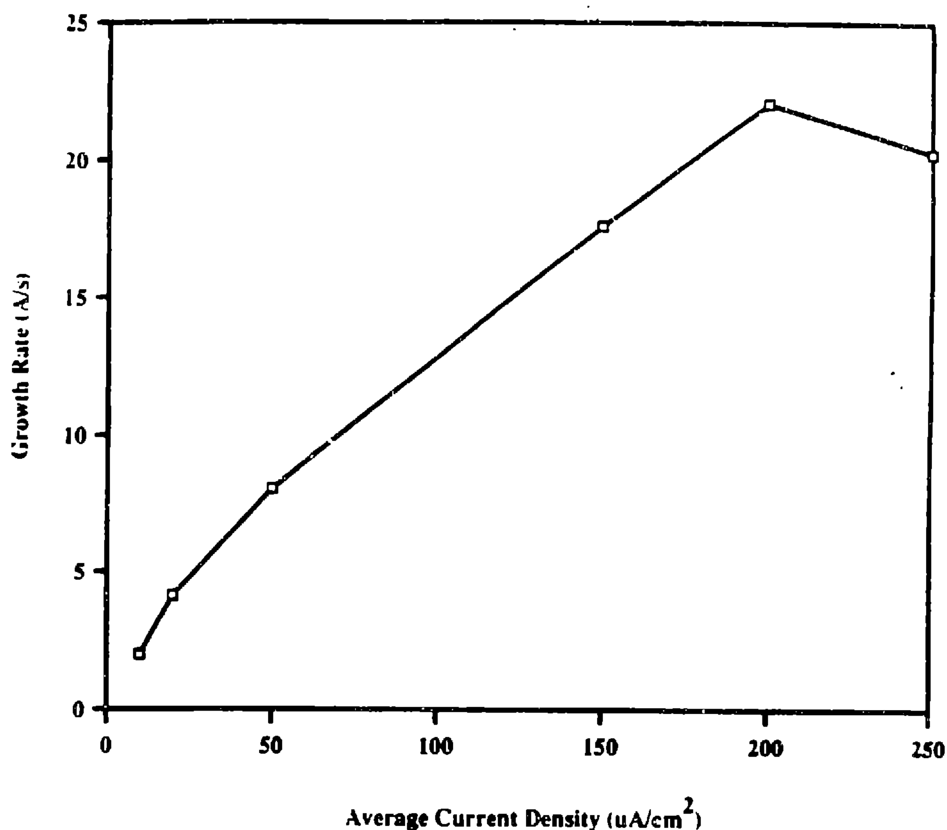

Figure 4-3: Growth rate in angstroms per second plotted as a function of the average ion current density. The depositions were made using 35 keV Ga^+ at room temperature at a gas precursor pressure of 1.5 mtorr at the point of ion incidence.

somewhat more quantitatively in a later section.

The yield data versus average current density can be expressed in another more useful form, namely the growth rate $G.R.$, defined as

$$G.R. = \frac{< J > Y_D(< J >)}{\rho_{at} e} \tag{4.2}$$

where the deposition yield $Y_D(< J >)$ is a function of the average current density $< J >$, ρ_{at} is the atomic density of copper (assuming that the film density is equal to that of pure bulk copper, 8.4 X 10^{22} atoms/cm^3), and e is the electronic charge. These results (figure 4-3) indicate that the growth rate increases and peaks at a much higher current density than that at which the maximum yield occurs, simply because the growth rate is the product of the yield and current density. The maximum growth rate is approximately 2.2 nm/s at a current density of 200 μA/cm^2. This rather high growth rate, compared to rates on the order of 0.2 to 1.5 nm/s for tungsten, gold, and

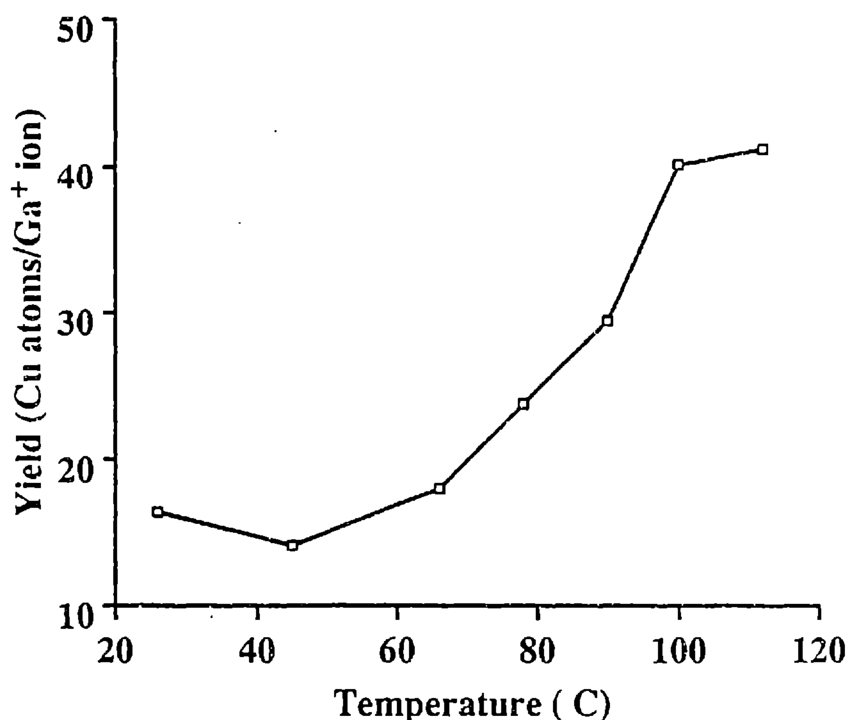

Figure 4-4: Deposition yield as a function of deposition temperature. The gas precursor pressure was about 1.5 mtorr and the average ion current density was 20 $\mu A/cm^2$, using 35 keV Ga^+.

platinum precursors[38, 27, 39] gives Cu(hfac)TMVS a distinct advantage in speed of deposition.

4.2.2 Temperature Dependence

The deposition yield of Cu(hfac)TMVS appears to be dependent on the substrate temperature, as indicated in figure 4-4 for an average ion current density of 20 $\mu A/cm^2$. This is to be expected, considering that the compound has been developed for organometallic CVD, which is carried out at elevated temperatures. Although the deposition yield was found to increase, no significant deposition was found outside of the irradiated area until the deposition temperature exceeded approximately 100°C, when some grains of copper were detected outside the ion-affected zone. It is likely that the combination of the ion flux and the higher temperature boosted the yield to a maximum of near 40 film atoms per incident ion near 110°C. Recall

that the Cu(hfac)TMVS compound is designed to spontaneously dissociate at temperatures above 120°C, but that some dissociation can occur at lower temperatures if water vapor is present on the sample.[30] An alternate explanation takes into account the product desorption, which would be hastened at higher temperatures. Since the byproduct molecules can escape the growing film more rapidly, it is possible that the deposition process can proceed faster as a result. For this explanation to be applicable, the increase in the growth rate due to product desorption must be significantly larger than the associated decrease in growth rate due to the desorption of unreacted Cu(hfac)TMVS molecules at the higher temperatures.

4.2.3 Dwell Time Dependence

The results of the experiments investigating the yield dependence on the scanning frequency, and hence on the ion beam dwell time, are presented in figure 4-5, for three different ion current densities. It is seen that a plateau region exists in the yield out to dwell times as long as 1 μs, at which point the yield begins to drop off; this characteristic is common to all three of the current densities sampled here. Since all the experiments investigating yield and resistivity as a function of temperature and current density were carried out at the extremely short dwell times in the range 10-100 ns, one may safely assume that only the temperature or current density effects on the deposition yield were seen in these runs and not the additional effects of yield attenuation due to depletion of the adsorbed gas, as outlined in the introductory chapter of this thesis. This result is significant because it means that under the gas flow conditions present in these experiment, the focused ion beam may be operated in the range 10 ns$< \tau_d <$1 μs without degrading the deposition yield.

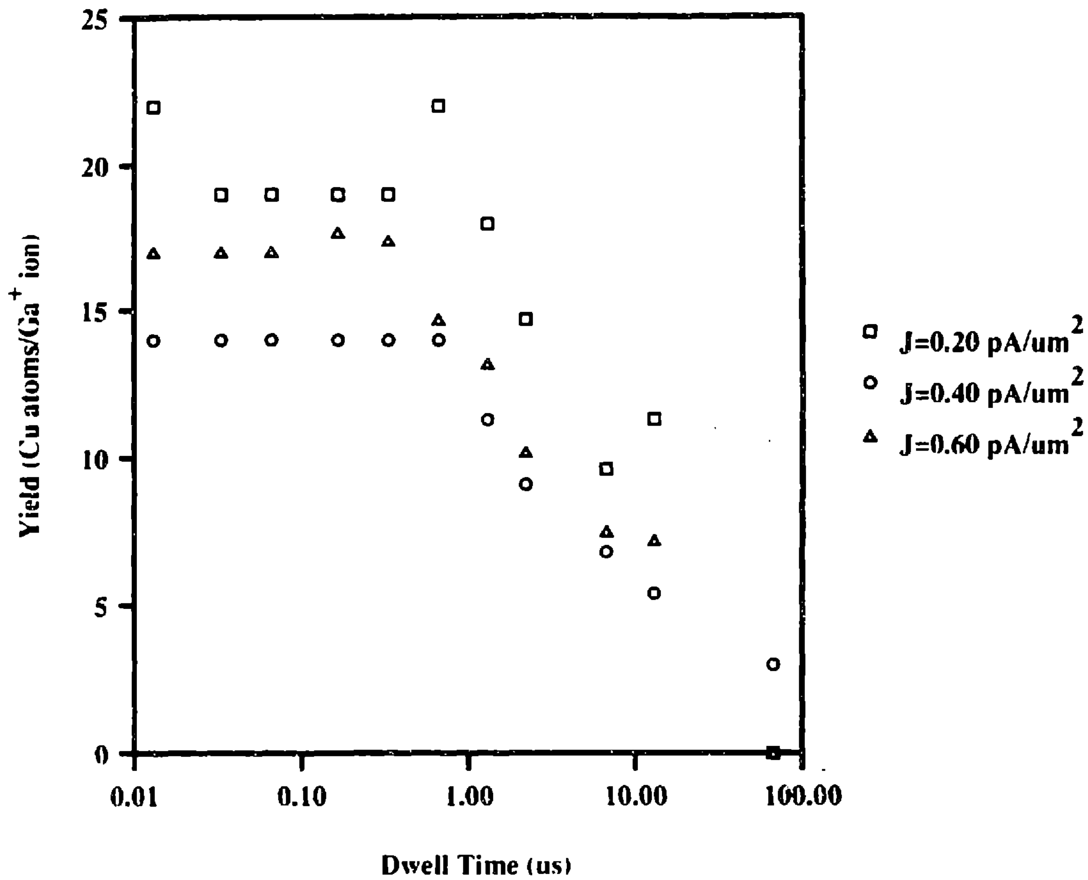

Figure 4-5: Dependence of the deposition yield on the ion beam dwell time. The depositions were all carried out using 35 keV Ga^+ at room temperature at a local precursor pressure of 1.5 mtorr. The average ion current density was varied as indicated in the graph.

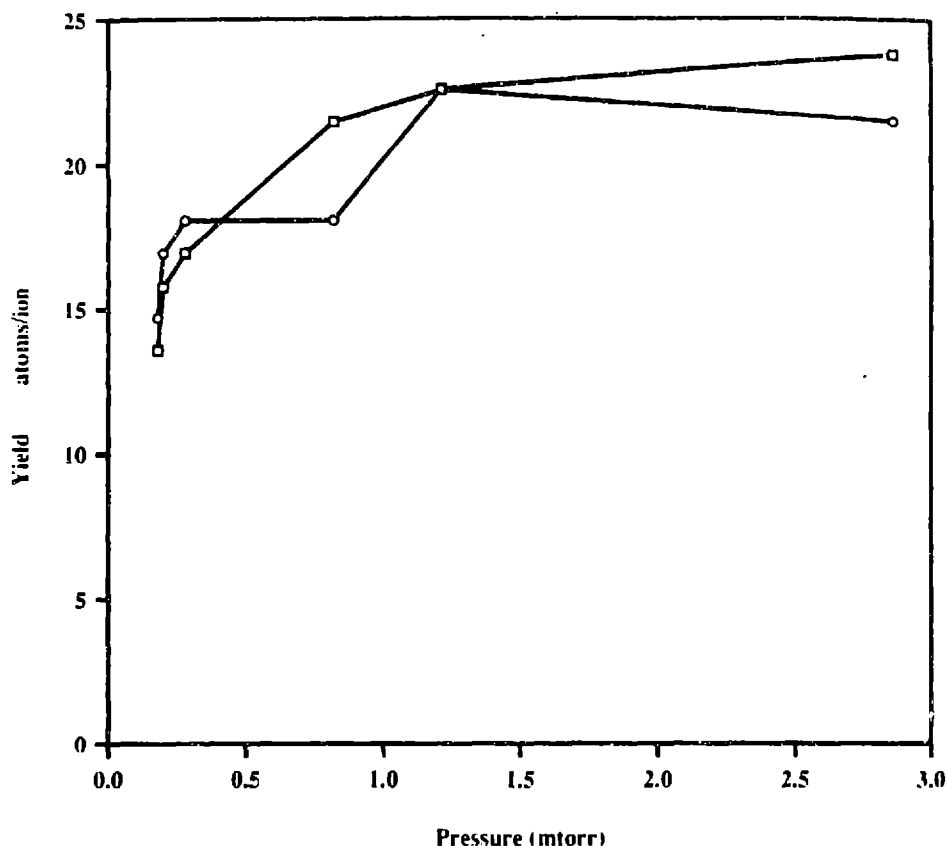

Figure 4-6: The deposition yield as a function of the local precursor gas pressure at the point of ion incidence, as measured via the stagnation tube experiment for two different experimental runs. The current density was 40 μA/cm^2 and the films were deposited using 35 keV Ga^+ at room temperature.

4.2.4 Pressure Dependence

Figure 4-6 illustrates the trend in yield as a function of the Cu(hfac)TMVS pressure. The pressure was varied by altering the distance between the sample and the capillary tube. An increase in yield is noted up to a certain point; the yield then apparently levels off to a constant value after approximately 1.25 mtorr. This behavior is typical of ion beam deposition when the precursor gas adsorbs in a monolayer on the surface of the sample.[28, 22]. The asymptotic value of the yield in this graph also correlates with the yield in figure 4-2 at a current density of 40 μA/cm^2. It is significant that even at low gas precursor pressures the deposition yield is still near 15 atoms/ion. This is to be contrasted with the relatively low yield of 5.5 atoms/ion for gold at similar pressures.[40]

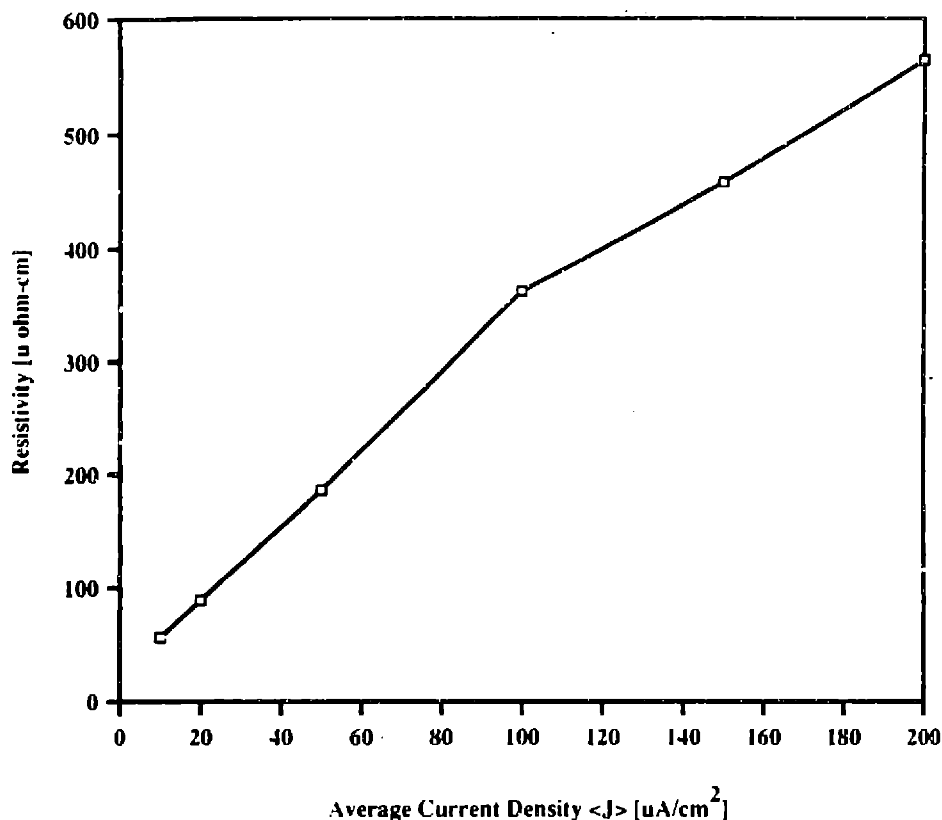

Figure 4-7: Resistivity of copper lines deposited on tungsten finger patterns (described in Chapter 3) versus average ion current density during deposition. The precursor pressure was approximately 1.5 mtorr at the sample surface and the lines were deposited at room temperature with 35 keV Ga^+. The resistivity of pure bulk copper is 1.67 $\mu\Omega$-cm.

4.3 Resistivity

4.3.1 Average Current Density Dependence

The resistivity versus current density plot appears in figure 4-7. An interesting aspect of this method of depositing copper films is that the resistivity measured via four-point-probe appears to be increasing with average ion current density; this behavior is distinctly different from, for instance, the platinum films grown from (MeCp)PtMe$_3$, which showed a decreasing resistivity with increasing gallium ion current density. As would be expected, the Pt films simultaneously became purer.[39] The composition of the copper films as a function of this deposition parameter will be discussed in a later section, but it is typical for the resistivity to serve as an indication of the purity of the metal: highly conductive metal films tend to be purer than films with resistivities

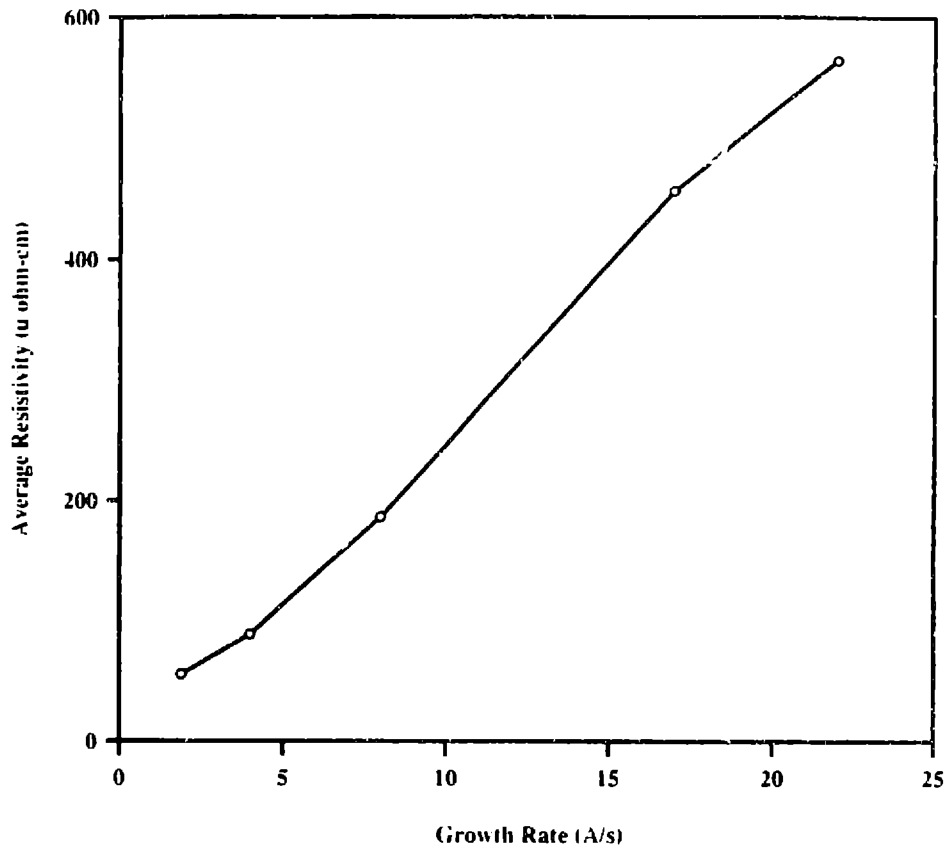

Figure 4-8: Resistivity plotted versus growth rate, illustrating the the decreasing conductivity trend. The local gas pressure was 1.5 mtorr and the lines were deposited at room temperature with 35 keV Ga^+.

many times higher than the pure, bulk value. In addition, the microstructure can also play a role in determining the value of the resistivity.

A graph of the resistivity values versus growth rate in figure 4-8 shows that the faster the film is growing, the less conductive it is. This may at first appear to be a discouraging result if the practical aim is to produce low resistance depositions in a short time, but in fact the decreasing conductivity is offset by the increasing, exceptionally high growth rate. Although the resistivity may be somewhat high at fast film growth rates, a deposited connector can be readily constructed with a large cross-sectional area to maintain an overall low resistance connection. This result suggests again that at the higher growth rates, the carbon-containing byproduct molecules (such as $Cu(hfac)_2$) lack the energy to escape the rapidly growing film at room temperature, giving more resistive films at higher ion current fluxes.

An investigation of the effect of changing the ion flux at a somewhat intermediate

$< J >$ (μA/cm^2) \ T (^oC)	25	40	67	80	100
5			○		
20	⊗	⊗	⊗	○	○
50	⊗		⊗		
150	×		×		
200	×				

Table 4.1: Schematic representation of regions of high and low resistivity as a function of current density $< J >$ and substrate temperature T. The circles represent low resistivity (20 $\mu\Omega$-cm and below), the x's represent high resistivity (150 $\mu\Omega$-cm and above), and the circled x's represent resistivities between these two values.

temperature of T=67° was also carried out. The result of all the resistivity measurements are very schematically represented in table 4.1. It is evident from the data points available that the high temperature and low growth rate (low ion current density) films tend to have a lower resistivity than those deposited at low temperature and high growth rate (high ion current density).

Table 4.2 is a comparison of the resistivities and growth rates of various focused ion beam deposited metals, specifically gold,[40] tungsten,[41] aluminum,[42] platinum,[43] and the copper investigated in this work. The column "F.O.M." contains the value of a figure of merit for these depositions, defined as Y/ρ, or the deposition yield divided by the resistivity; the usefulness and quality of the deposited material for integrated circuit repair is then directly proportional to the magnitude of this quantity. In the leftmost column is the time needed to deposit a feature with a resistance of 100 Ω and a size of 10 μm^2, or a sheet resistance of 10 $\Omega/\square$. It is

Metal (Precursor)	Resistivity ($\mu\Omega$-cm)	Yield (atoms/ion)	F.O.M. (atoms/$\mu\Omega$-cm-ion)	Growth Rate (Angstroms/s)	Time to deposit 100 Ω feature (min)
Au (DMG(hfac))	500	4	8 x 10^3	10	7.9
W ($W(CO)_6$)	190	2	1.1 x 10^4	4.9	6.4
Al (TMMA)	900	5	5.6 x 10^3	1.3	11.5
Pt ((MeCp)$PtMe_3$)	490	2.5	5.1 x 10^3	5.9	13.8
Cu (Cu(hfac)TMVS)	550	10	1.8 x 10^4	18	5

Table 4.2: Comparative Deposition Characteristics at an Average Ion Current Density of 250 $\mu A/cm^2$.

evident that the copper deposited from Cu(hfac)TMVS exhibits the highest figure of merit and consequently requires the shortest time to deposit the feature described.

4.3.2 Temperature Dependence

Figure 4-9 depicts the effects of stage heating during focused ion beam induced deposition of copper. A precipitous drop in resistivity is noted between 70 and 80°C, which seems to be connected more with the change in microstructure in this temperature regime than with a change in composition. Both of these characteristics of the film will be discussed more thoroughly in a later section. It should be noted that the highest deposition temperatures, at 100°C and above, yielded films with resistivities on the same order of magnitude as pure copper, which has a resistivity of 1.7 $\mu\Omega$-cm.

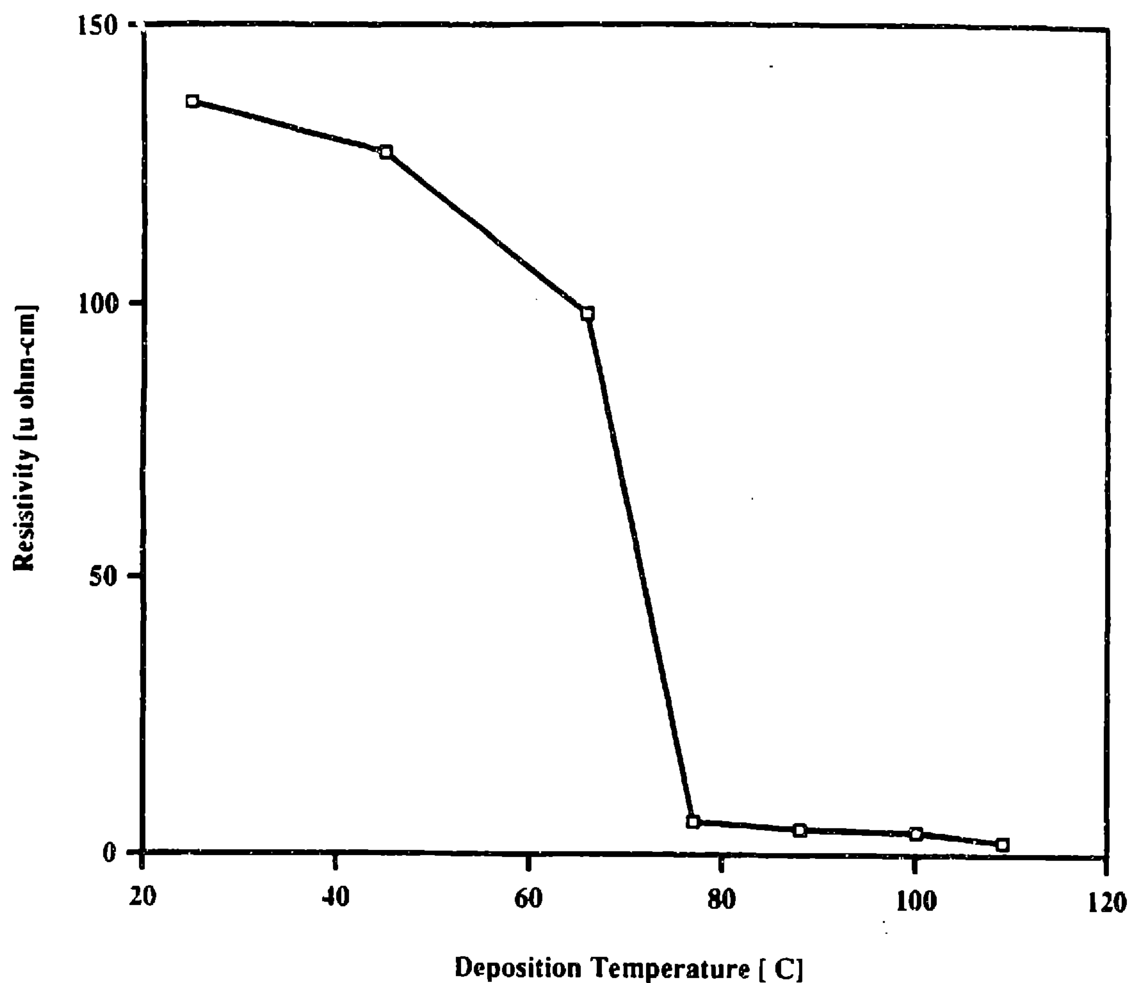

Figure 4-9: Effect of increasing deposition temperature on the film resistivity. The resistivity at the highest temperature is approximately 2 $\mu\Omega$-cm, close to the value for pure copper (1.7 $\mu\Omega$-cm). The films were deposited at a local precursor pressure of about 1.5 mtorr at an average ion current density of 20 $\mu A/cm^2$ using 35 keV Ga^+.

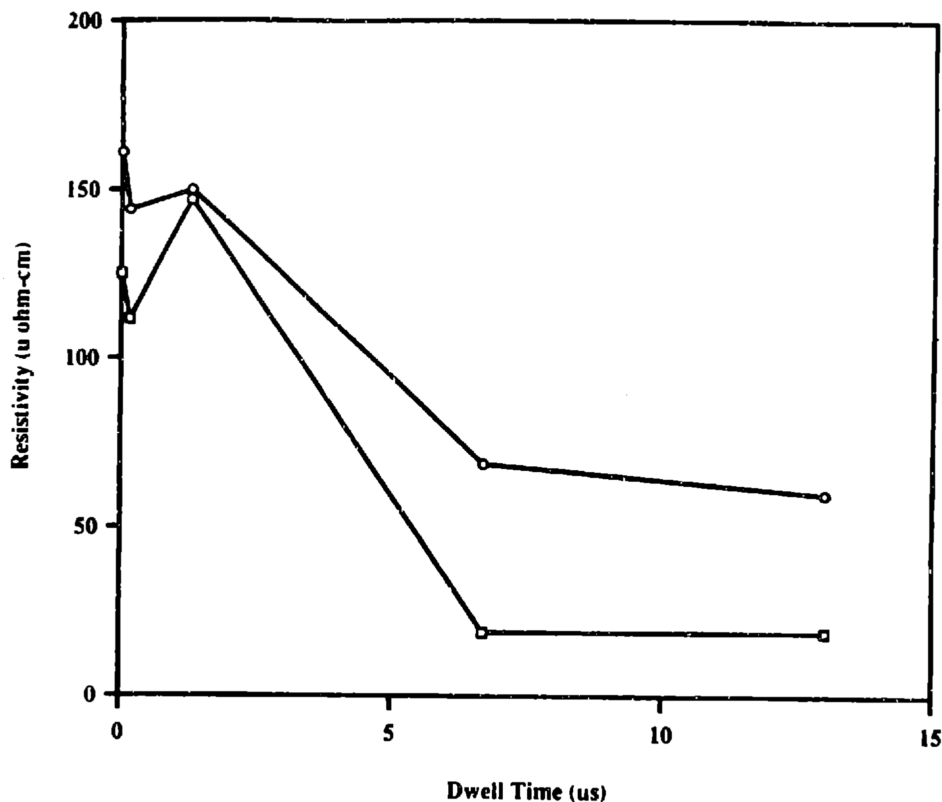

Figure 4-10: Effect of varying dwell time on resistivity of copper depositions using 35 keV Ga^+. The local gas pressure was approximately 1.5 mtorr, at an ion current density of 40 $\mu A/cm^2$. The two curves show the results of two experimental runs.

4.3.3 Dwell Time Dependence

The effects of dwell time variation on the resistivity of the copper depositions is depicted in figure 4-10. An interesting trend of increasingly conductive copper lines was discovered at longer dwell times, with a concurrent decrease in deposition yield discussed in the previous section. It is possible that a form of beam-induced annealing is taking place at longer ion beam dwell times although no Auger analysis was done on these particular samples to confirm this. An alternative explanation is that with the reduction in yield and the concomitant decrease in growth rate, the reaction byproducts can more readily escape the film, resulting in a purer, less resistive material.

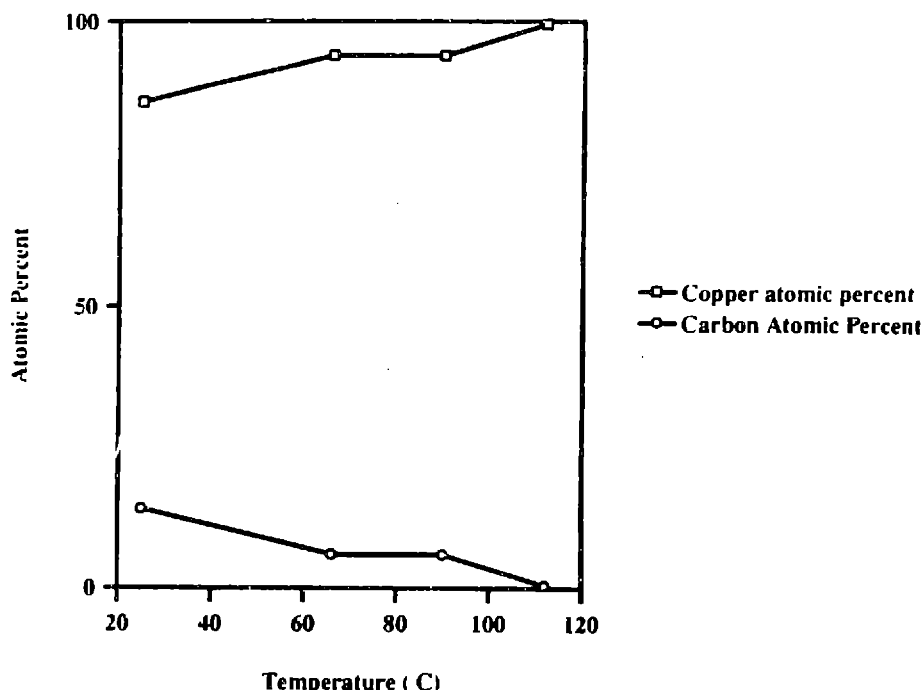

Figure 4-11: Composition of copper films deposited using 35 keV Ga^{+} at various sample temperatures. The gas pressure was 1.5 mtorr during deposition, and the ion current density was 20 $\mu A/cm^2$.

4.4 Composition

4.4.1 Temperature Dependence

Using a resistively heated stage, it was possible to deposit films at a range of temperatures and then examine the composition dependence on temperature using Auger Electron Spectroscopy (AES). These results are presented in figure 4-11, and exhibit a characteristic similar to gold films deposited from DMG(hfac), in that the relative fraction of the metallic component increases with increasing deposition temperature, i.e. the hotter the stage, the purer the film. The primary contaminant in the copper films, as in the gold, was found to be carbon. At room temperature, the copper content was found lie between 50 and 80 atomic percent, with the remainder chiefly carbon from the reaction byproducts. At the highest temperatures, the film was found to be nearly pure copper, with negligible amounts of contaminants such as carbon,

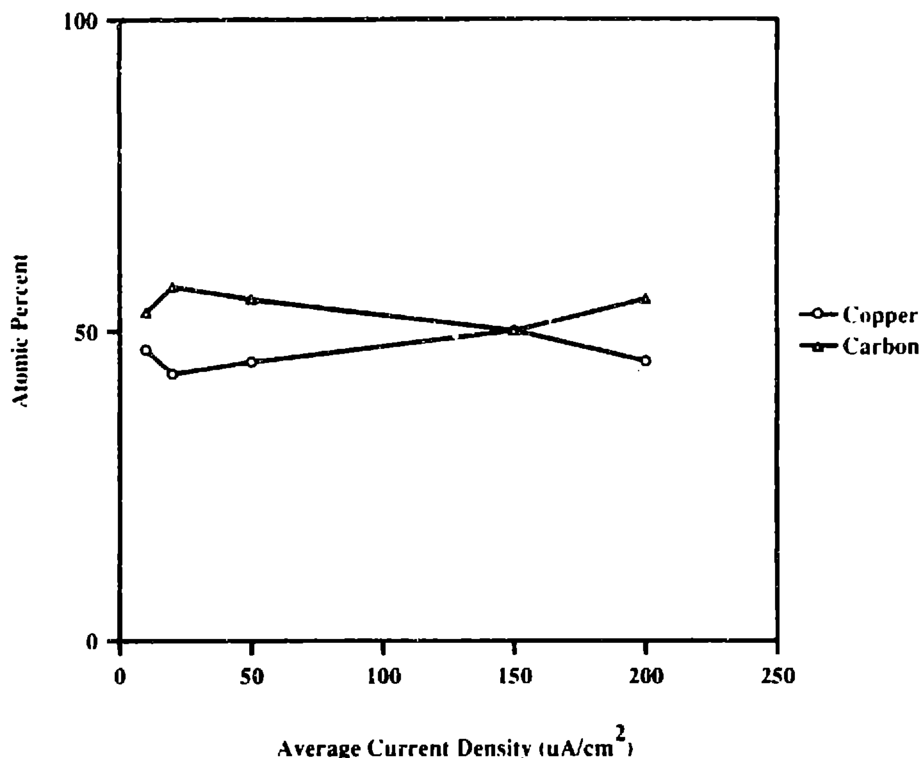

Figure 4-12: Composition of copper films deposited at various average ion current densities, as determined using Auger Electron Spectroscopy. The local precursor pressure was approximately 1.5 mtorr, and the films were deposited at room temperature with 35 keV Ga^+.

oxygen, and gallium. One must note that at the highest temperature, some loss of selectivity was noted in the area immediately surrounding the ion irradiated patch in the form of small granules of copper. These granules did not, however, form a continuous film of any appreciable thickness.

4.4.2 Average Current Density Dependence

As depicted in figure 4-12, the major components of the copper deposition are copper and carbon. Oxygen and gallium were found in trace amounts but not to a significant extent. The remarkable feature of this composition probe is that the relative amounts of carbon and copper in the film remain relatively constant from 10 to 200 $\mu A/cm^2$ ion current density. The film appears to be composed largely of a 1:1 copper:carbon atomic ratio regardless of the ion current density. This is strikingly different from the results of gold deposition from DMG(hfac), where the metal content of the films was

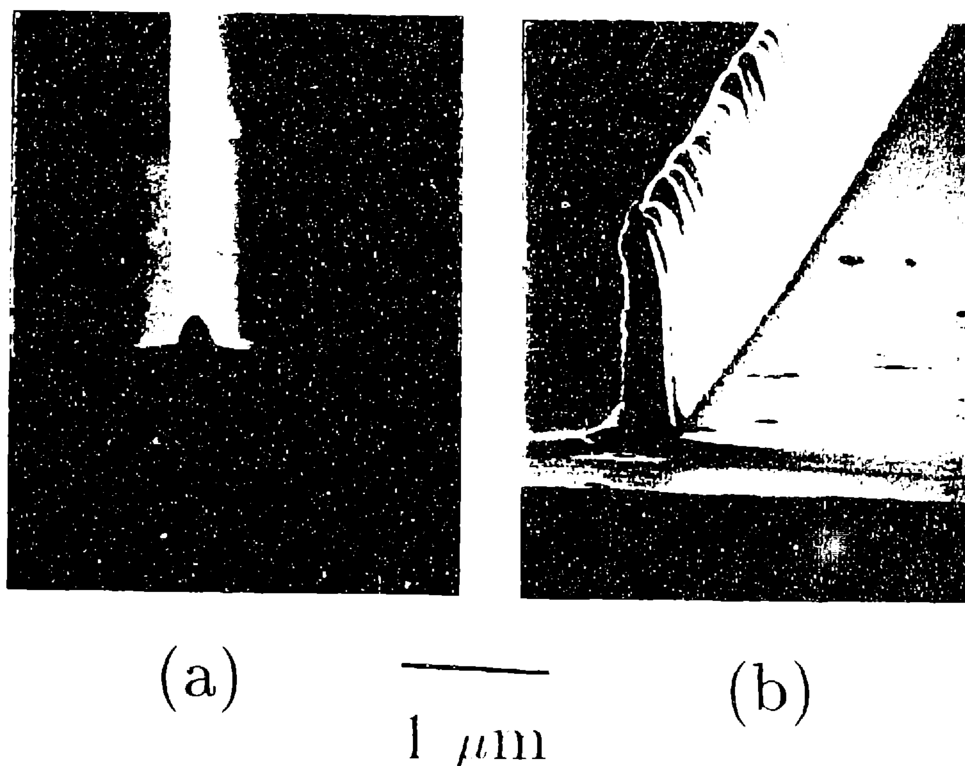

Figure 4-13: SEM micrographs of copper lines deposited at an ion current density of (a) 110 $\mu A/cm^2$ for 1 minute and (b) 128 $\mu A/cm^2$ for 10 minutes using 25 keV Ga^+.

found to increase with increasing ion current density as measured using AES.[40] The carbon content of the copper films in these runs appears to be greater than that of the films deposited at different temperatures, probably due to degradation of some of the Cu(hfac)TMVS precursor over a period of several months into $Cu(hfac)_2$. This, however, should not effect the results achieved at high temperatures, nor did it affect the resistivities of the films at room temperature.

4.5 Microstructure

4.5.1 High Aspect Ratio Lines

It is possible to achieve reasonably high aspect ratio growth using this copper precursor compound. Figure 4-13 depicts submicron copper lines grown using the Cu(hfac)TMVS compound using the FEI FIB 500D machine. The smallest linewidths were achieved on this machine, which gave lines of approximately 0.25 μm width, as seen in the

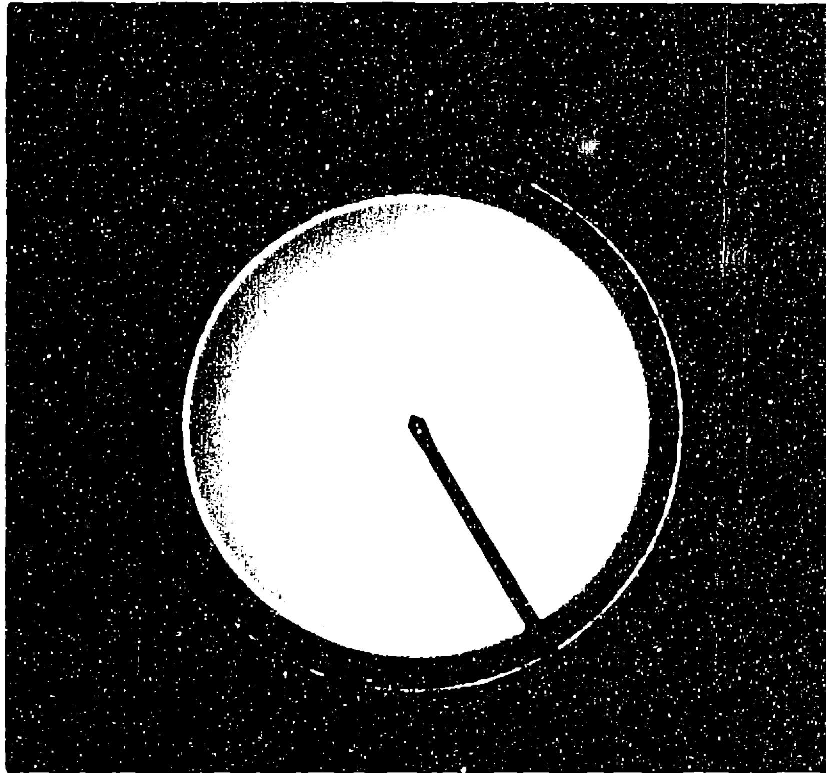

Figure 4-14: Electron diffraction pattern from a film deposited with 25 keV Ga^+ at 80^oC, at a precursor pressure of 1.5 mtorr and an ion current density of 20 $\mu A/cm^2$.

figure. Aspect ratios of 5.4 to 1 have been achieved.

4.5.2 Temperature Dependence

As an indication of the crystallographic structure of the film, an electron diffraction pattern appears in figure 4-14. The sharp rings denote that the film is polycrystalline copper, so we may presume that these copper films exhibit a morphology very similar to that of the ion induced gold depositions, or a polycrystalline film composed of metal islands in a matrix of impurities at low deposition temperatures. In comparison, the focused ion beam deposited films of platinum were found to be amorphous.[39]

The temperature dependence of the microstructure of the copper films was found to be very similar to that of the gold films deposited using FIB from the compound DMG(hfac).[28, 44] When deposited at room temperature (figure 4-15(a)), the microstructure consists of small islands of copper, approximately 20 nm in size, embedded in a matrix which is probably largely carbon, as suggested by Auger Electron

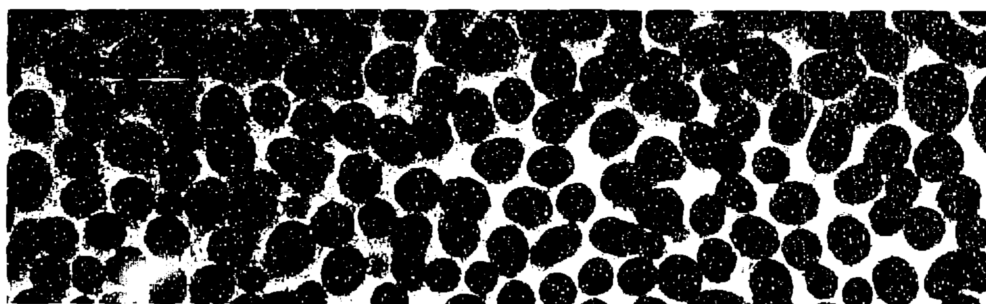

(a) 25°C

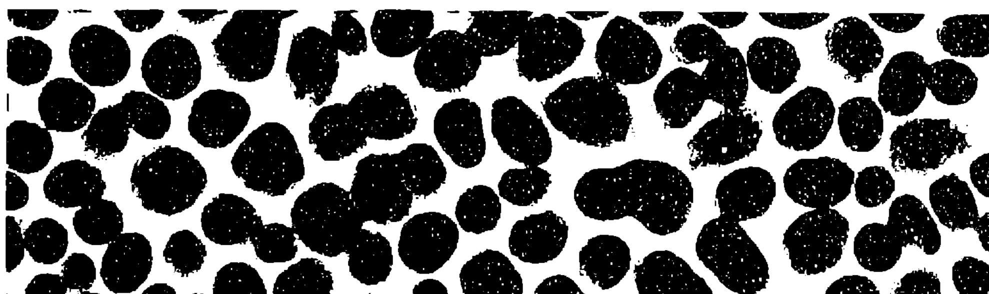

(b) 40°C

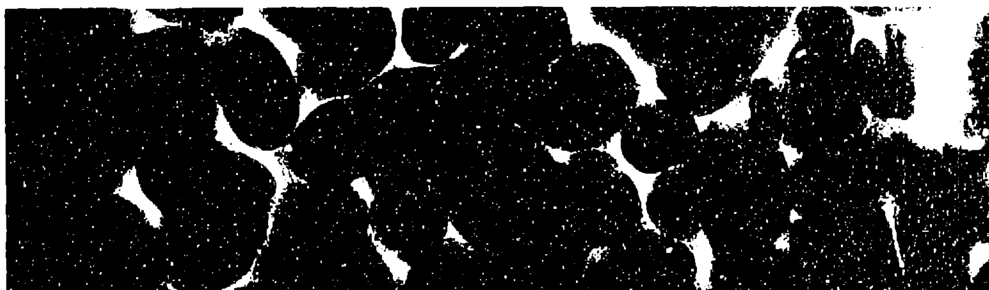

(c) 67°C

25 nm

Figure 4-15: TEM micrographs of approximately 50 nm thick FIBID copper films deposited using 25 keV Ga^{+} at (a) room temperature, (b) 40°C, (c) 67°C, (d) 80°C, and (e) 100°C. The average current density during deposition was 20 $\mu A/cm^2$ of 25 keV Ga^{+} at a local precursor pressure of about 1.5 mtorr.

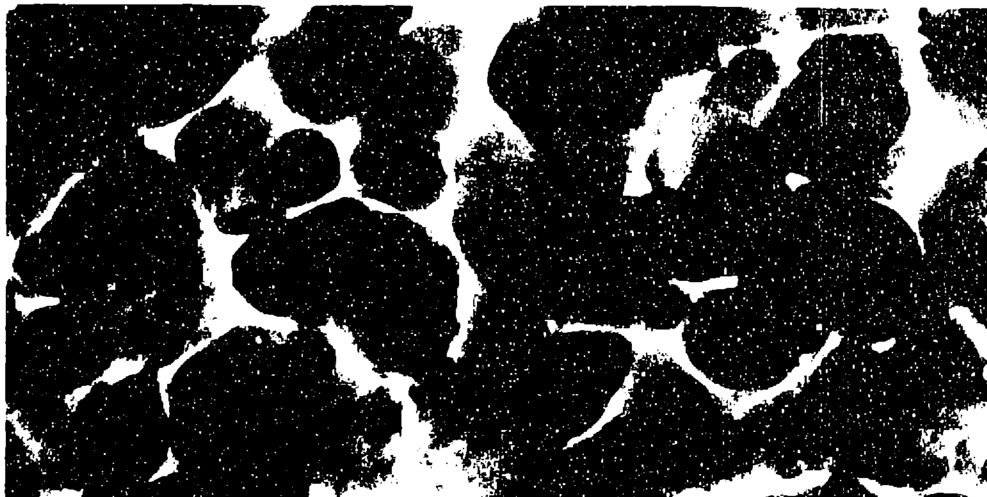

(d) 80°C

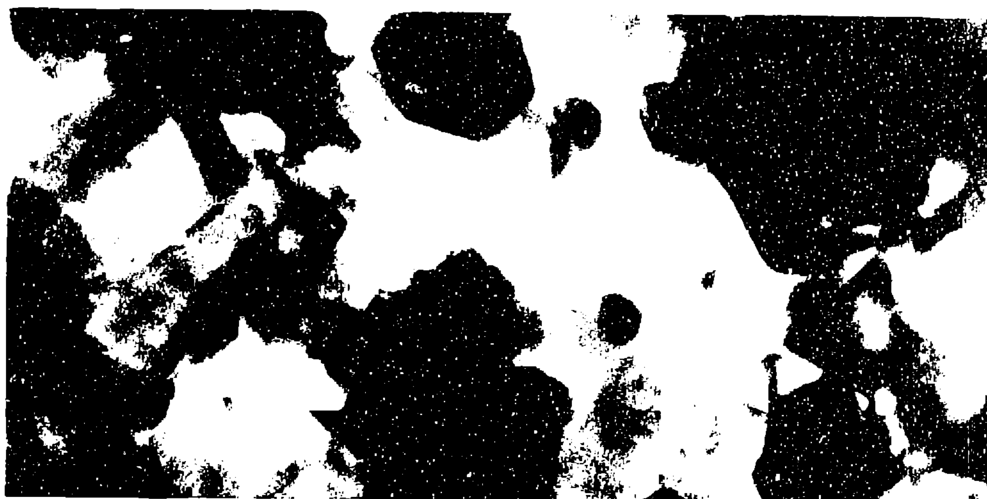

(e) 100°C

25 nm

Figure 4-15: (continued)

Spectroscopy. At a slightly higher temperature (figure 4-15(b)), some enlargement of the copper islands is observed, but they are still non-contiguous and distinct and form a non-percolating structure. Deposition at a somewhat higher temperature (figure 4-15(c)) of 67°C results in a significant enlargement of the copper islands to the point that they begin to impinge on one another. It is at this point that the resistivity drops to a value more characteristic of a metal. Further heating of the substrate, as in figures 4-15(d) and (e) causes the film to become more continous and percolate until the resistivity approaches that of bulk, pure copper. The microstructure in the last case appears to be devoid of the carbon matrix which characterizes the deposition at low temperatures and seems to be a typical metal film composed of contiguous grains of about 0.1 μm in size.

SEM micrographs of the surface morphology reveal structures in agreement with the TEM micrographs (figure 4-16). Low temperature films have a relatively smooth surface. Increasing the deposition temperature results in a rougher topography, until the highest temperature film reveals grain-like structures on the surface which appear to be the same approximate size as those grains observed using TEM.

4.5.3 Average Current Density Dependence

TEM micrographs of the copper films deposited at increasingly intense ion fluxes at room temperature appear in figure 4-17. The microstructural evolution in this case is not similar to that exhibited by focused ion beam deposited gold deposited at different ion current densities. In the case of gold, the metallic islands were found to grow significantly and impinge on one another at current densities close to 200 $\mu A/cm^2$. [28] Here the increasing ion current only causes a very modest growth, by perhaps a factor of two in island size. This is much less drastic than the island growth observed as a result of an increase in the temperature during deposition, which caused an island or grain size increase of approximately a factor of five to ten. One should note that the islands are still not contiguous at the highest ion current density. SEM photographs in figure 4-18 confirm that the roughening of the surface is not marked.

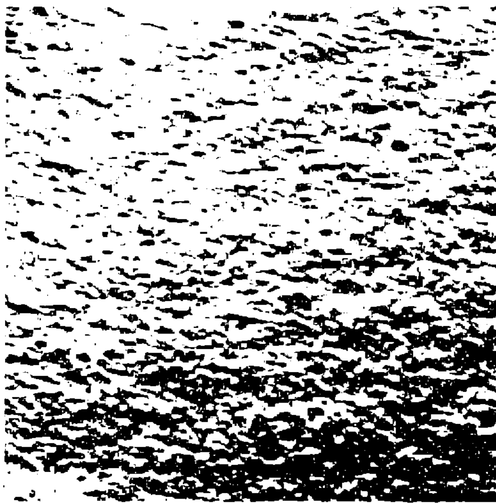

(a) 25°C

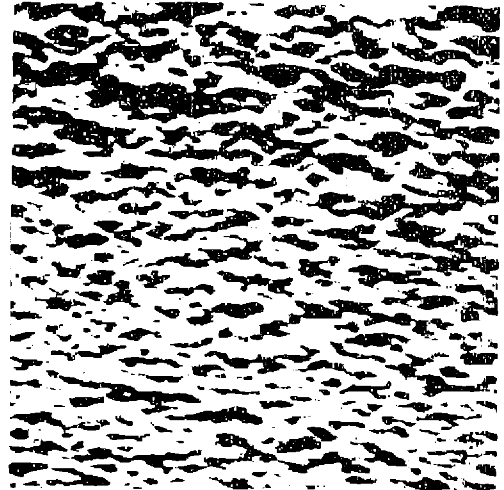

(b) 66°C

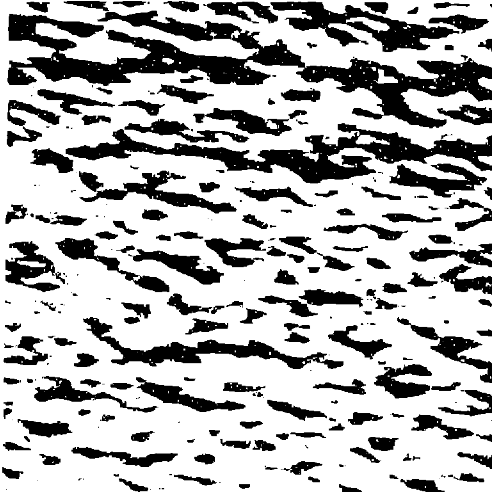

(c) 78°C

1 μm

(d) 100°C

Figure 4-16: SEM micrographs of FIBID copper films illustrating the roughening of the surface at higher deposition temperatures using 35 keV Ga^+. (a) room temperature, (b) 66°C (c) 78°C (d) 100°C. The films were deposited at an ion current density of 20 $\mu A/cm^2$ at a precursor pressure of 1.5 mtorr.

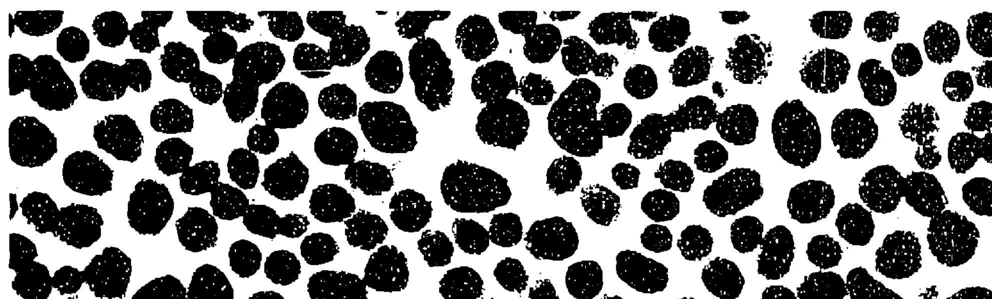

(a) 10 μA/cm^2

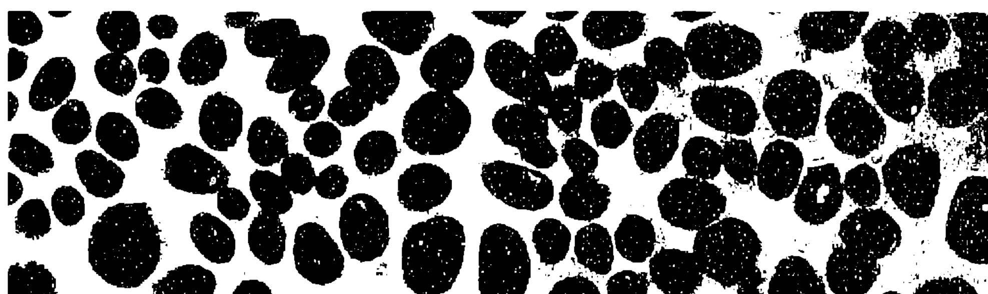

(b) 50 μA/cm^2

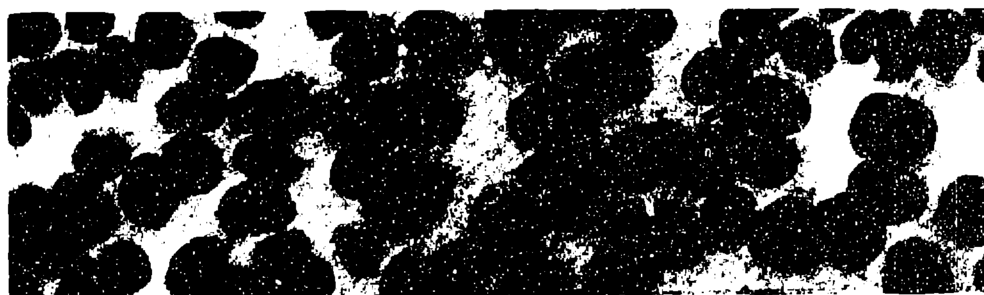

(c) 200 μA/cm^2

25 nm

Figure 4-17: TEM micrographs of approximately 50 nm thick FIBID copper films deposited with 25 keV Ga^+ at average ion current densities of (a) 10 μA/cm^2, (b) 50 μA/cm^2, and (c) 200 μA/cm^2. The films were deposited at room temperature at a local precursor pressure of 1.5 mtorr.

(a) 20 μA/cm^2

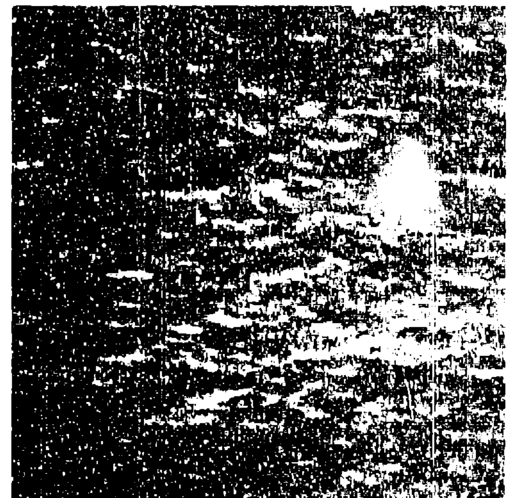

(b) 50 μA/cm^2

(c) 200 μA/cm^2

0.75 μm

Figure 4-18: SEM micrographs of FIBID copper films deposited with 35 keV Ga^+ at different average ion current densities, illustrating the surface morphology. (a) 20 μA/cm^2, (b) 50 μA/cm^2, and (c) 200 μA/cm^2. The films were deposited at room temperature at a local precursor pressure of 1.5 mtorr.

4.5.4 Dwell Time Dependence

A comparison of films deposited at increasingly long dwell times appear in figure 4-19 in plan-view. The film seems to show some slight degree of island growth at the longer dwell time. At the longer time of τ_d =2.2μs, the film is somewhat thinner due to the reduced yield at long ion beam dwell times. Once again, it is not immediately obvious why this microstructure might result in lower resistivity material as determined by four-point-probe testing, but the most convincing explanation connects this trend with a decrease in the growth rate. There is no Auger composition data for these samples, but it is possible that the films are purer at the lower growth rates associated with longer ion beam dwell times. The effect of dwell time on the composition and resistivity of the ion beam deposited gold films was not explored [28, 22] so no comparison can be made between the copper and gold films.

4.5.5 Precursor Pressure Dependence

TEM Micrographs of the copper films at decreasing precursor gas pressure at the point of ion incidence (figure 4-20) indicates that there is little change in the copper microstructure with pressure. This is distinctly different from the general trend observed in ion beam induced deposition of gold; the texture of the gold films at lower gas pressures showed an increasingly rough surface, with larger grain-like features observed at 0.1 mtorr DMG(hfac) pressure than at a 10 mtorr pressure. [28] The explanation for this is that at higher precursor pressures, the fully adsorbed layer of precursor gas molecules prevents the carbon-containing reaction byproducts from desorbing, resulting in increased carbon incorporation and impeded metal island growth; the resultant islands are small and non-contiguous. At low precursor gas pressures, the precursor gas molecules no longer adsorb in a full monolayer at the surface and a larger number of the reactant byproduct molecules can escape; the islands can then grow to a larger size, unimpeded by carbon and other impurities. It is possible that for the Cu(hfac)TMVS, the growth rate is still very high even at incomplete precursor adsorption, resulting in increased carbon incorporation and prevention of island

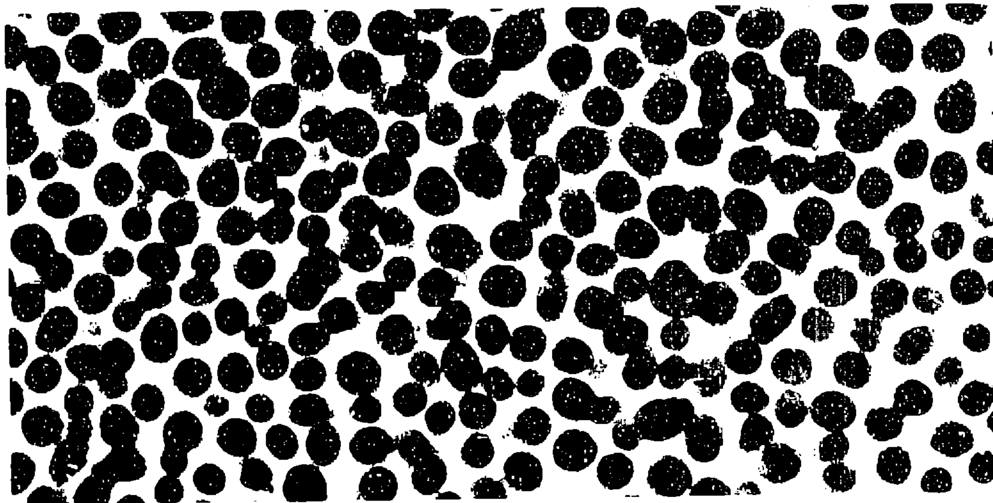

(a) 100 ns

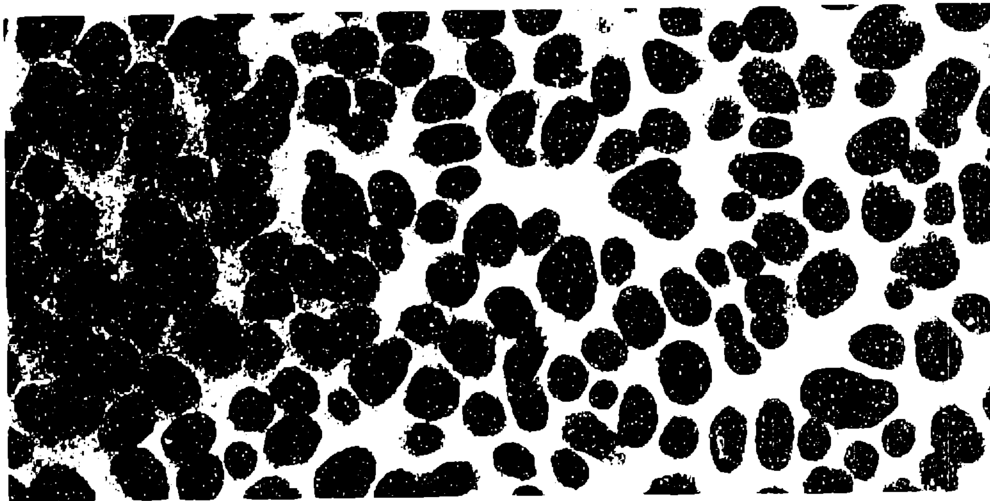

(b) 2.2 μs

25 nm

Figure 4-19: TEM micrographs of approximately 50 nm thick FIBID copper films deposited at ion beam dwell times of (a) 100 ns and (b) 2.2 μs The films were deposited at room temperature at a current density of 20 $\mu A/cm^2$, at a local precursor pressure of 1.5 mtorr

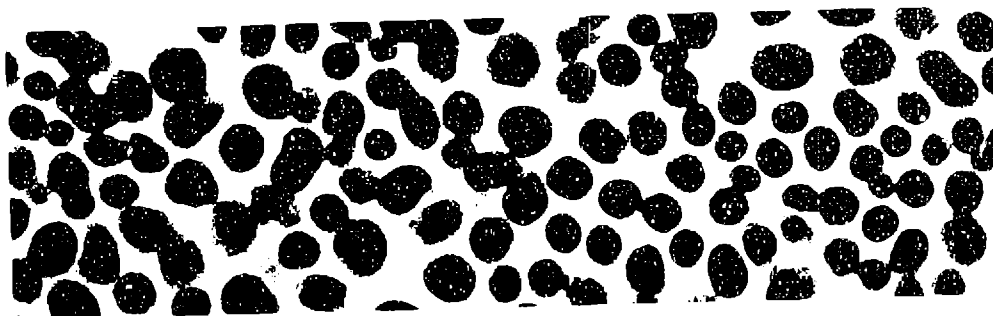

(a) 2.6 mtorr

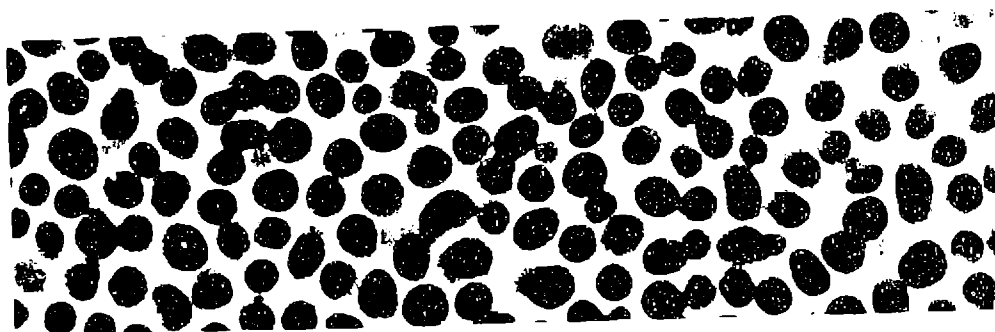

(b) 1.5 mtorr

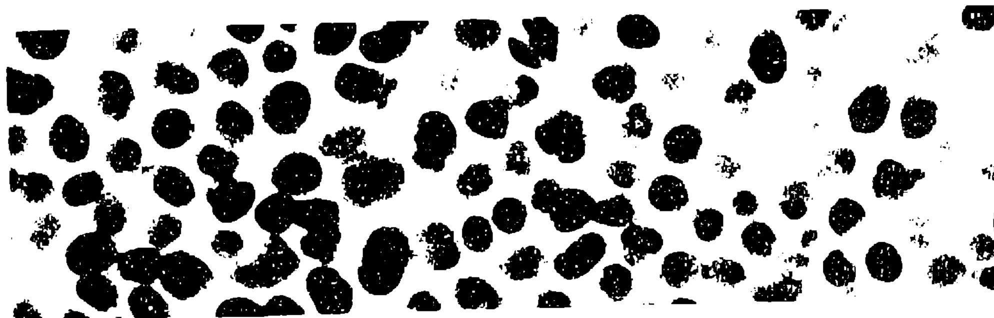

(c) 0.25 mtorr

25 nm

Figure 4-20: TEM micrographs of approximately 50 nm thick FIBID copper films deposited at local Cu(hfac)TMVS pressures of (a) 2.6 mtorr (b) 1.5 mtorr and (c) 0.25 mtorr. The films were deposited at room temperature at a current density of 20 $\mu A/cm^2$.

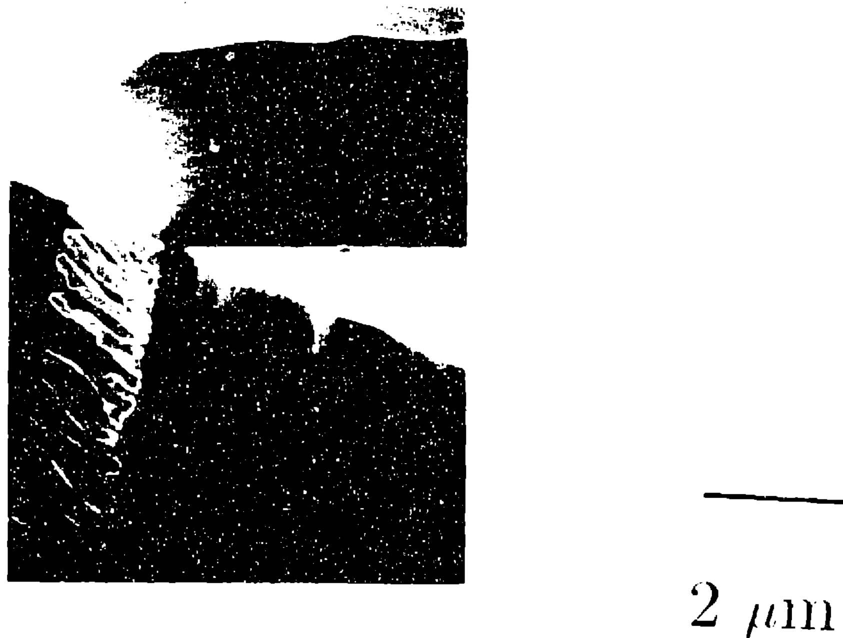

Figure 4-21: Example of periodic comb-like structure as the ion beam deposits on a nearly vertical sidewall. The line was deposited at room temperature at an ion current density of 250 $\mu A/cm^2$.

impingement and percolation.

4.5.6 Sidewall Deposition

An interesting feature observed during depositions on a steep sidewall was the formation of a quasi periodic comb-like structure (figure 4-21). This type of structure has been observed in platinum, tungsten, and gold focused ion beam induced depositions at glancing angles of ion incidence.[14, 39] It is believed to be the result of shadowing of growing film nuclei by other nuclei, causing preferential growth; the leading edge of a particular "blade" on the comb is believed to create a shadow in the ion flux for a certain distance behind it; at this point the next nucleus can grow into a blade and similarly create its own shadow. From this qualitative explanation is is possible to imagine how this quasi-periodic structure arises at high angles of ion incidence.

4.6 Summary

This chapter detailed the experimental results in the areas of film growth, restivity and purity, and microstructure. The measurements of Cu(hfac)TMVS precursor pressure was related to the yield measurements. TEM and SEM photographs of the films indicate a purer, coarser, polycrystalline film at higher temperatures, but little change in microstructure was observed as a result of increasing current density, ion beam dwell time, or precursor pressure.

Chapter 5

Conclusions and Future Work

5.1 Summary and Conclusions of this Work

The most striking characteristic of the focused ion beam deposited copper from the Cu(hfac)TMVS precursor compound seems to be the high yield and growth rate of this compound. A maximum yield of 28 atoms/ion (or 14 copper atoms/ion when corrected for composition as determined by Auger analysis) is measured for an average ion beam current density of 20 $\mu A/cm^2$, but the maximum growth rate of 2.2 nm/s in the range of current densities studied so far appears at 200 $\mu A/cm^2$. Another important trend observed is the increasing resistivity observed with more intense ion flux, from a value near 50 $\mu\Omega$-cm at low current densities to over ten times as high at current densities near 200 $\mu A/cm^2$. Because the growth rate is increasing so rapidly while the resistivity is increasing, the higher resistivity does not pose much of an obstacle to the creation of low resistance jumpers and interconnects in integrated circuit repair; a jumper of sufficiently large cross section can be deposited in a reasonable amount of time. In this respect, the deposition of copper from this compound seems feasible for use in this capacity as long as an effective diffusion barrier can be interposed between the copper films and the underlying, active silicon devices. An investigation of yield as a function of precursor gas pressure and ion beam dwell time demonstrates a decreasing yield with decreasing pressure (decreasing organometallic flux) and increasing dwell time, as would be expected from the dwell time model

discussed in chapter 1 of this thesis.

The exploration of the microstructure shows that the most drastic change in film morphology occurs with the change in deposition temperature. Temperatures near room temperature give rise to metallic islands embedded in a low density matrix presumably composed chiefly of carbon. The island size at low temperatures tends to be about 20 nm. An increase in the stage temperature during deposition leads to gradual impingement of the islands until they become contiguous grains, a factor of 5 to 10 greater in size. A concomitant decrease in the carbon content is detected by Auger analysis until at the highest deposition temperatures, between 100°C and 110°C, the film becomes almost 100 atomic percent copper and exhibits a resistivity within experimental error of pure copper (1.7 $\mu\Omega$-cm). As the ion current density is increased to about 200 $\mu A/cm^2$, the copper islands grow slightly, but not as dramatically as in the case of higher deposition temperatures. The Auger results indicate that films deposited at room temperature at increasingly intense ion fluxes do not change in composition, but tend to remain in a 1:1 copper:carbon atomic ratio. The increase in film resistivity in such films may be tied into a microstructural effect not revealed by the plan-view TEM micrographs; perhaps an increasingly discontinuous, non-columnar island structure would be visible in cross-section. An alternate explanation is that the the film is growing too rapidly to desorb carbon, especially at the more intense ion fluxes. Additionally, the microstructure is not found to vary drastically with precursor gas pressure, and only a slight coarsening is observed with increasing ion beam dwell time. The relative lack of variation in island size with precursor gas pressure may be a reflection once again of the high growth rate of this compound; decreasing the local precursor pressure consequently does little to assist in the desorption of carbon-containing byproduct molecules, resulting in little or no coarsening of the copper islands. In the case of increased dwell time, the slight island growth that is observed is corroborated by a decrease in resistivity of the film, which usually typifies an increasingly coarse microstructure.

The quality of the copper films deposited using this compound seems to be inextricably tied to the ability of the product molecules (i.e. $Cu(hfac)_2$ and TMVS,

for instance) to escape from the growing film. The evidence of higher yield with increasing temperature, increasing resistivity with higher growth rate, and TEM micrographs and Auger data all point to the conclusion that a higher quality deposition is obtained when the the desorption of carbon-containing byproduct molecules is rapid compared to the growth rate of the film. This condition can be most readily achieved by either using extremely low ion current densities at room temperature or by heating the sample.

5.2 Future Work

Certainly there is room for a good amount of additional work in this subject area. A more complete characterization of the microstructure of this focused ion beam deposited metal could be carried out by studying a large area of variable space, i.e. a map of microstructure as a function of two important variables such as temperature and average ion current density or ion current and ion beam dwell time could be constructed. In addition, Auger composition and resistivity data for each point in the variable space would also be useful in delimiting ranges of the parameters giving the highest quality films. A more thorough study of the microstructure might be carried out via cross-sectional TEM. This would be an exceedingly difficult procedure for the small patches of focused ion beam deposited material discussed here, but cross-sectional TEM samples of large patches of copper film deposited in a conventional broad-beam ion implanter would be more convenient to examine. It is possible that any microstructural causes underlying the increasing resistivity trend with increasing ion flux might be revealed with this kind of data. An additional area which might be pursued would be the deposition of thin, narrow seed lines of copper using the focused ion beam. Selective organometallic chemical vapor deposition could then be carried out to create high aspect ratio lines of very high purity and, consequently, with resistivities close to the pure copper value in a short time. Perhaps a more rigorous investigation of the desorption characteristics of the carbon-containing byproducts of the Cu(hfac)TMVS reaction should be undertaken to isolate ways of drastically

improving the film quality. The problem of copper diffusion through underlying dielectrics would need to be addressed in both the focused ion beam and organometallic CVD modes of film growth before the technique could become acceptable for use in silicon integrated circuits, but the technique as explored in this work seems promising.

Bibliography

[1] William B. Glendinning and John N. Helbert, editors. *Handbook of VLSI Microlithography.* Noyes Publications, Park Ridge, N.J., 1991.

[2] Wayne M. Moreau. *Semiconductor lithography: principles, practices and materials.* Plenum Press, New York, 1988.

[3] David J. Elliott. *Microlithography: Process Technology for IC Fabrication.* McGraw-Hill, New York, 1986.

[4] Arnost Reiser. *Photoreactive Polymers: The Science and Technology of Resists.* Wiley, New York, 1989.

[5] R. Clampit, K.L. Aitken, and D.K. Jefferies. *J. Vac. Sci. Tech.*, 12, 1208 (1975).

[6] R. Clampit and D.K. Jefferies. *Nucl. Instrum. Methods*, 142, 739 (1978).

[7] J.H. Orloff and L.W. Swanson. *J. Vac. Sci. Tech.*, 12, 1209 (1975).

[8] J.H. Orloff and L.W. Swanson. *J. Vac. Sci. Tech.*, 15, 845 (1978).

[9] J. Melngailis. *J. Vac. Sci. Tech. B*, 5(2), 469 (1987), and references therein.

[10] R. Levi-Setti. *Adv. Electron. Electron Phys. Suppl.*, A13, 261 (1980).

[11] J.W. Ward, M.W. Utlaut, and R.L. Kubena. *J. Vac. Sci. Tech. B*, 5, 169 (1987).

[12] K.D. Cummings, L.R. Harriott, G.C. Chi, and F.W. Ostermayer Jr. *SPIE*, 632, 93 (1986).

[13] C.R. Musil, J.L. Bartelt, and J. Melngailis. *IEEE Electron Dev. Lett.*, EDL-7, 285 (1986).

[14] X. Xu, A. Della Ratta, J. Sosonkina, and J. Melngailis. *J. Vac. Sci. Tech. B*, 10(6), 2675 (1992).

[15] R. Kubena, R.L. Seliger, and E.H. Stevens. *Thin Solid Films*, 92, 165 (1982).

[16] J. Melngailis, P.G. Blauner, A.D. Dubner, J.S. Ro, T. Tao, and C.V. Thompson. *Second International Symposium on Process Physics and Modelling*, p. 653, 1990.

[17] K. Nikawa, K. Nasu, M. Murase, T. Kaito, T. Adachi, and S. Inoue. *1989 International Reliability Physics Symposium, 27th annual proceedings*, p.1, 1989).

[18] J.E. Jensen. *Solid State Tech.*, 27, 145 (1984).

[19] M. Komuro, N. Atoda, and H. Kawakatsu. *J. Electrochem. Soc.*, 126, 483 (1979).

[20] K. Gamo, K. Moriizumi, M. Ochiai, M. Takai, S. Namba, T. Shiokawa, and T. Minamisono. *Jpn. J. Appl. Phys.*, 23, L642 (1984).

[21] K. Gamo, G. Huang, K. Moriizumi, N. Samoto, R. Shimizu, and S. Namba. *Nucl. Instrum. Meth. Phys. Res.*, B 7/8, 864 (1985).

[22] A.D. Dubner. *Mechanism of ion beam induced deposition.* Ph.D. Thesis, MIT (1990).

[23] A.D. Dubner, A. Wagner, J. Melngailis, and C.V. Thompson. *J. Appl. Phys.*, 70, 665 (1991).

[24] J.P Biersack and L.G. Haggmark. *Nucl. Instrum. Methods*, 174, 257 (1980).

[25] J.P. Biersack and W.G. Eckstein. *Appl. Phys. A*, 34, 73 (1984).

[26] G.M Shedd, H. Lezec, Dubner A.D., and J. Melngailis. *Appl. Phys. Lett.*, 49, 1584 (1986).

[27] P.G. Blauner, J.S. Ro, Y. Butt, and J. Melngailis. *J. Vac. Sci. Tech.*, 7, 609 (1989).

[28] J.S. Ro. *Microstructure and mechanism of gold films grown by ion beam induced deposition.* Ph.D. Thesis, MIT (1991).

[29] Y. Takahashi, Y. Madokoro, and T. Ishitani. *Jpn. J. Appl. Phys.*, 30, 3233 (1991).

[30] J.A.T. Norman, B.A. Muratore, P.N. Dyer, D.A. Roberts, A.K. Hochberg, and L.H. Dubois. Presented at E-MRS Meeting, Strasbourg, France, June, 1992.

[31] J.A.T. Norman, B.A. Muratore, P.N. Dyer, D.A. Roberts, and A.K. Hochberg. *Journal de Physique*, IV, C2-271 (1991).

[32] S.M. Sze, editor. *VLSI Technology.* McGraw-Hill, New York, 1988.

[33] J.W. Mayer and L.C. Feldman. *Fundamentals of Surface and Thin Film Analysis.* North-Holland, New York, 1986.

[34] S.K. Ghandi. *VLSI Fabrication Principles.* Wiley, New York, 1985.

[35] D. Chescoe and P.J. Goodhew. *The Operation of Transmission and Scanning Electron Microscopes.* Oxford University Press, Oxford, 1990.

[36] A.W. Agar, R.H. Alderson, and D. Chescoe. *Principles and Practice of Electron Microscope Operation.* North-Holland, Amsterdam, 1974.

[37] P.G. Blauner, Y. Butt, J.S. Ro, C.V. Thompson, and J. Melngailis. *J. Vac. Sci. Tech.*, B7 (6), 1816 (1989).

[38] Z. Xu, T. Kosugi, K. Gamo, and S. Namba. *J. Vac. Sci. Tech.*, B7, 1959 (1989).

[39] T. Tao, J.S. Ro, and J. Melngailis. *J. Vac. Sci. Tech.*, B8(6), 1826 (1990).

[40] P.G. Blauner, J.S. Ro, Y. Butt, C.V. Thompson, and J. Melngailis. In *MRS Symposium Proceedings*, Vol. 129, p. 483, 1989.

[41] D.K. Stewart, L.A. Stern, and J.C. Morgan. *SPIE*, (1989).

[42] M.E. Gross, L.R. Harriott, and R.L. Opila. *J. Appl. Phys.*, 68, 4820 (1990).

[43] J. Puretz and L.W. Swanson. *J. Vac. Sci. Tech. B*, 10(6), 2695 (1992).

[44] J.S. Ro, A.D. Dubner, C.V. Thompson, and J. Melngailis. In *MRS Symposium Proceedings*, Vol. B101, 1987.